

Development of a Trans-dimensional Fault Slip Inversion for Geodetic Data

Fumiaki Tomita¹, Takeshi Iinuma¹, Ryoichiro Agata¹, and Takane Hori¹

¹Japan Agency for Marine-Earth Science and Technology

November 24, 2022

Abstract

Geodetic fault slip inversions have been generally performed by employing a least squares method with a spatial smoothing constraint. However, this conventional method has various problems: difficulty in strictly estimating non-negative solutions, assumption that unknowns follow the Gaussian distributions, unsuitability for expressing spatially non-uniform slip distributions, and high calculation cost for optimizing many hyper-parameters. Here, we have developed a trans-dimensional geodetic slip inversion method using the reversible-jump Markov chain Monte Carlo (rj-MCMC) technique to overcome the problems. Because sub-fault locations were parameterized by the Voronoi partition and were optimized in our approach, we can estimate a slip distribution without the spatial smoothing constraint. Moreover, we introduced scaling factors for observational errors. We applied the method to the synthetic data and the actual geodetic observational data associated with the 2011 Tohoku-oki earthquake and found that the method successfully reproduced the target slip distributions including a spatially non-uniform slip distribution. The method provided posterior probability distributions with the unknowns, which can express a non-Gaussian distribution such as large slip with low probability. The estimated scaling factors properly adjusted the initial observational errors and provided a reasonable slip distribution. Additionally, we found that checkerboard resolution tests were useful to consider sensitivity of the observational data for performing the rj-MCMC method. It is concluded that the developed method is a powerful technique to solve the problems of the conventional inversion method and to flexibly express fault-slip distributions considering the complicated uncertainties.

1
2
3
4
5
6
7
8
9
10
11
12
13
14
15
16
17

Development of a Trans-dimensional Fault Slip Inversion for Geodetic Data

F. Tomita¹, T. Iinuma¹, R. Agata¹, T. Hori¹

¹Research Institute for Marine Geodynamics, Japan Agency for Marine-Earth Science and Technology

Corresponding author: Fumiaki Tomita (tomitaf@jamstec.go.jp)

†Additional author notes should be indicated with symbols (current addresses, for example).

Key Points:

- Trans-dimensional geodetic inversion method was developed and applied to synthetic tests and data for the 2011 Tohoku-oki earthquake
- The developed method can express a spatially non-uniform slip distribution and uncertainties for unknowns following non-Gaussian distributions
- The developed method can appropriately adjust scaling factors for the observational errors

18 **Abstract**

19 Geodetic fault slip inversions have been generally performed by employing a least squares
20 method with a spatial smoothing constraint. However, this conventional method has various
21 problems: difficulty in strictly estimating non-negative solutions, assumption that unknowns
22 follow the Gaussian distributions, unsuitability for expressing spatially non-uniform slip
23 distributions, and high calculation cost for optimizing many hyper-parameters. Here, we have
24 developed a trans-dimensional geodetic slip inversion method using the reversible-jump Markov
25 chain Monte Carlo (rj-MCMC) technique to overcome the problems. Because sub-fault locations
26 were parameterized by the Voronoi partition and were optimized in our approach, we can
27 estimate a slip distribution without the spatial smoothing constraint. Moreover, we introduced
28 scaling factors for observational errors. We applied the method to the synthetic data and the
29 actual geodetic observational data associated with the 2011 Tohoku-oki earthquake and found
30 that the method successfully reproduced the target slip distributions including a spatially non-
31 uniform slip distribution. The method provided posterior probability distributions with the
32 unknowns, which can express a non-Gaussian distribution such as large slip with low
33 probability. The estimated scaling factors properly adjusted the initial observational errors and
34 provided a reasonable slip distribution. Additionally, we found that checkerboard resolution tests
35 were useful to consider sensitivity of the observational data for performing the rj-MCMC
36 method. It is concluded that the developed method is a powerful technique to solve the problems
37 of the conventional inversion method and to flexibly express fault-slip distributions considering
38 the complicated uncertainties.

39

40 **1 Introduction**

41 Precise estimation on fault slip distributions is important to understand slip behaviors
42 during earthquake cycles. Geodetic slip inversions have been generally conducted to estimate
43 fault slip distributions, and a conventional geodetic slip inversion is performed by a least squares
44 method (LSM). In this conventional approach, a smoothing constraint on fault-slips (e.g.,
45 Laplacian regulation) is generally provided to avoid overfitting. Then, strength of smoothing is
46 determined by a criteria such as a trade-off L-curve [e.g., Du et al., 1992] and Akaike's Bayesian

47 Information Criterion (ABIC) [e.g., Yabuki & Matsu'ura, 1992]. However, some problems in the
48 LSM-based geodetic slip inversion have been noted: (1) it is difficult to strictly impose a direct
49 constraint (such as non-negative constraint) [Fukuda & Johnson, 2008], (2) it is difficult to
50 evaluate estimation error when unknowns follow non-Gaussian distributions, (3) it is unsuitable
51 for estimating a spatially heterogeneous fault slip distribution because spatially uniform
52 smoothing is applied, and (4) it takes effort to adjust the hyper-parameters when the multiple
53 hyper-parameters are introduced, such as weighting hyper-parameters for multiple data and
54 smoothing hyper-parameters for multiple time-windows in the viscoelastic inversion [Tomita et
55 al., 2020].

56 To overcome the above problems, various approaches have been developed. Although
57 LSMs without using the simple Laplacian regulation have been investigated, such as utilizing
58 spectral decomposition [e.g., Hori, 2001; Jin et al., 2007; Xu et al., 2018] and promoting sparse
59 solutions [e.g., Evans & Meade, 2012], they are not suitable for solving problems (1) and (2).
60 Meanwhile, slip inversion methods using a Markov chain Monte Carlo (MCMC) technique have
61 been well developed recently [e.g., Fukuda & Johnson, 2008; Minson et al., 2013]. MCMC-
62 based slip inversions can treat a direct constraint strictly and express posterior probability
63 distributions of model parameters [Fukuda & Johnson, 2008]. Furthermore, they can provide
64 posterior probability distributions of hyper-parameters as well as those of the model parameters
65 [e.g., Fukuda & Johnson, 2008; Kubo et al., 2016], which is an useful solution for the problem
66 (4). Thus, MCMC is a useful technique to solve the problems (1), (2), and (3). Although most of
67 the previous MCMC-based slip inversion studies have introduced the Laplacian regulation as
68 similar to the LSM-based slip inversions, MCMC-based slip inversions without using the
69 Laplacian regulation have been recently developed to solve the problem (3). One approach is that
70 the number and size of sub-faults are optimized based on the spatial resolution of observational
71 data prior to the MCMC sampling [Kimura et al., 2019]; however, a spatially smooth fault slip
72 distribution cannot be resolved by this method. Another idea is introduction of a complicated
73 regulation such as von Karman regulation [e.g., Amey et al., 2018].

74 Here, we investigated a trans-dimensional geodetic slip inversion method using a
75 reversible jump MCMC (rj-MCMC) technique [Green, 1995]. Through the trans-dimensional
76 approach, number of model parameters is automatically adjusted based on the sensitivity of
77 observational data and model complexity. Among the applications of the trans-dimensional

78 approach to geophysics [e.g., Bodin & Sambridge, 2009; Hawkins & Sambridge, 2015], spatial
79 model parameters are divided into groups by a parameterization technique (e.g., Voronoi
80 partition, Figure 1). For the Voronoi partition parameterization, model space is discretized using
81 the Voronoi nuclei (Figure 1), and number and spatial positions of the nuclei are optimized
82 through rj-MCMC sampling [Bodin and Sambridge, 2009]. Considering this optimization, the
83 trans-dimensional approach can be regarded as a sparse modeling method. As indicated by Bodin
84 and Sambridge [2009], ensemble of the rj-MCMC samples can express spatially smooth
85 distribution of the model parameters without any smoothing constraints. Furthermore, weighting
86 hyper-parameters for multiple observation data can be introduced in the rj-MCMC technique in
87 the same manner as conventional MCMC techniques [e.g., Dettmer et al., 2014]. Thus, we
88 expect that the trans-dimensional approach overcomes all of the above problems.

89 For geophysical studies, the trans-dimensional approach has been often applied to explore
90 underground geophysical structures using seismic wave data [e.g., Bodin & Sambridge, 2009;
91 Bodin et al. 2012] and electrical resistivity data [e.g., Galetti & Curtis 2018]. Furthermore, the
92 approach has been also applied to estimate tsunami sources due to a large subduction earthquake
93 [Dettmer et al., 2016]. However, there are few applications of the approach to estimate fault slip
94 distributions; for example, Dettmer et al. [2014] and Hallo and Gallovič [2020] investigated a
95 fault slip distribution using seismic wave data. Although Amey et al. [2019] estimated a fault slip
96 distribution using geodetic observational data, they utilized the rj-MCMC technique and a von
97 Karman regulation together to restrict the number of sub-faults with non-zero slip. Thus, the
98 application of the trans-dimensional geodetic slip inversion has not been well investigated.

99 One of the characteristics of the geodetic slip inversion is that we often treat many types of
100 observational data such as onland GNSS, onland InSAR, offshore GNSS-Acoustic (GNSS-A),
101 offshore bottom pressure (OBP), and the others. Determination of relative weights among these
102 various data is an important issue [e.g., Funning et al., 2014]; however, it is difficult optimized
103 the relative weights by conventional inversion approaches because of computational costs when
104 types of the observational data are many. This study tried to automatically adjust many
105 weighting hyper-parameters through the MCMC sampling process. Moreover, compared with
106 other geophysical data, the geodetic data have heterogeneity of spatial coverage of observational
107 sites: dense onshore sites and sparse offshore sites. This heterogeneity provides strong spatial
108 variation of sensitivity to fault slips. We expect that the rj-MCMC method can consider such

109 spatil variation of the data sensitivity because fault patch sizes are variable depending on the
 110 observational data. Thus, this study tried investigated how the rj-MCMC method works for
 111 various patterns of the observational sites.

112 In this study, we performed a simple trans-dimensional geodetic slip inversion using the
 113 rj-MCMC method based on the Voronoi partition through synthetic tests and an application to
 114 actual observational data associated with the 2011 Tohoku-oki earthquake. We then assessed
 115 utility of the trans-dimensional inversion approach for analyzing geodetic observational data.

116

117 2 Methods

118 2.1 Observation equation

119 We aim to analyze geodetic observational data with multiple time windows or from
 120 multiple observational instruments. An observational equation that links the vector of ground
 121 surface displacements \mathbf{d} with the vector of fault slips \mathbf{s} via the matrix of Green's functions \mathbf{G} is:

$$\mathbf{d} = \mathbf{G}\mathbf{s} + \mathbf{e}, \quad (1)$$

122 where \mathbf{e} is an observational error vector. When we have I types of the observational data and J
 123 components of fault slips (hereafter, called as fault-slip component), Equation (1) is re-written as
 124 follows:

$$\begin{pmatrix} \mathbf{d}_1 \\ \vdots \\ \mathbf{d}_I \end{pmatrix} = \begin{pmatrix} \mathbf{G}_{1,1} & \cdots & \mathbf{G}_{1,J} \\ \vdots & \ddots & \vdots \\ \mathbf{G}_{I,1} & \cdots & \mathbf{G}_{I,J} \end{pmatrix} \begin{pmatrix} \mathbf{s}_1 \\ \vdots \\ \mathbf{s}_J \end{pmatrix} + \begin{pmatrix} \mathbf{e}_1 \\ \vdots \\ \mathbf{e}_I \end{pmatrix}; \quad (2)$$

125 for example, if we estimate fault slips in horizontally orthogonal slip directions for coseismic
 126 slip, $J = 2$, or if we estimate fault slips in horizontally orthogonal slip directions for transient
 127 slip with three time windows, $J = 2 \times 3$.

128 We consider the observational error vector \mathbf{e} obeys an observational covariance matrix \mathbf{E} .
 129 The observational covariance matrix can be expressed by combination of I types of the
 130 observational covariance matrices $\mathbf{E}_i (i = 1, \dots, I)$ as

$$\mathbf{e} \sim \mathbf{E} = \begin{pmatrix} \mathbf{E}_1 & \mathbf{0} & \mathbf{0} \\ \mathbf{0} & \ddots & \mathbf{0} \\ \mathbf{0} & \mathbf{0} & \mathbf{E}_I \end{pmatrix}. \quad (3)$$

131 Most of the previous geodetic inversion studies fixed the observational covariance matrix
 132 initially given from instrumental measurement errors. However, considering modeling errors and
 133 the difficulty in assessing instrumental measurement errors, it is reasonable to introduce scale
 134 factors to the individual types of the observational covariance matrices [e.g., Dettmer et al.,
 135 2014; Funning et al., 2014]. According to Dettmer et al. [2014], we provided hierarchical scaling
 136 parameters, $\lambda_i^2 (i = 1, \dots, I)$, which multiplies the initial observational covariance matrices
 137 $\mathbf{E}_i^{\text{ini}} (i = 1, \dots, I)$. As each hierarchical scaling parameter is a positive value, we transformed λ_i^2
 138 into $10^{-\Lambda_i}$ and sampled $\Lambda_i (i = 1, \dots, I)$ in same manner as Kubo et al. [2016] (hereafter, Λ is
 139 called as a weighting parameter). Then, Equation (3) is re-written as

$$\mathbf{e} \sim \mathbf{E} = \begin{pmatrix} \mathbf{E}_1 & \square & \mathbf{0} \\ \square & \ddots & \square \\ \mathbf{0} & \square & \mathbf{E}_I \end{pmatrix} = \begin{pmatrix} \lambda_1^2 \mathbf{E}_1^{\text{ini}} & \square & \mathbf{0} \\ \square & \ddots & \square \\ \mathbf{0} & \square & \lambda_I^2 \mathbf{E}_I^{\text{ini}} \end{pmatrix} = \begin{pmatrix} 10^{-\Lambda_1} \mathbf{E}_1^{\text{ini}} & \square & \mathbf{0} \\ \square & \ddots & \square \\ \mathbf{0} & \square & 10^{-\Lambda_I} \mathbf{E}_I^{\text{ini}} \end{pmatrix}. \quad (4)$$

140 Subsequently, defining $\mathbf{W}_i^{\text{ini}} = \mathbf{E}_i^{\text{ini}-1}$, the weight matrix is written as

$$\mathbf{W} = \begin{pmatrix} 10^{\Lambda_1} \mathbf{W}_1^{\text{ini}} & \square & \mathbf{0} \\ \square & \ddots & \square \\ \mathbf{0} & \square & 10^{\Lambda_I} \mathbf{W}_I^{\text{ini}} \end{pmatrix}. \quad (5)$$

141

142 2.2 Principle of the rj-MCMC method

143 In the Bayesian framework, all information on unknowns can be expressed by the
 144 probability density function (PDF). From Bayes theorem [Bayes, 1763], a posterior PDF of
 145 unknowns \mathbf{x} when data \mathbf{d} are given can be written as

$$p(\mathbf{x} | \mathbf{d}) = \frac{p(\mathbf{d} | \mathbf{x})p(\mathbf{x})}{p(\mathbf{d})} \propto p(\mathbf{d} | \mathbf{x})p(\mathbf{x}) \quad (6)$$

146 where $p(\mathbf{d} | \mathbf{x})$ is a likelihood function of observational data \mathbf{d} given \mathbf{x} , and $p(\mathbf{x})$ is the a priori
 147 PDF of \mathbf{x} . The posterior PDF can be written by a proportionality relationship using $p(\mathbf{d} | \mathbf{x})$ and
 148 $p(\mathbf{x})$ because $p(\mathbf{d})$, which is evidence indicating a priori PDF of \mathbf{d} , is independent of \mathbf{x} [e.g.,
 149 Sambridge et al., 2006]. In an ordinary MCMC approach (e.g., the Metropolis-Hasting (MH)
 150 algorithm [Metropolis et al., 1953; Hastings, 1970]), unknowns are updated based on a posterior
 151 PDF. As for the MH algorithm, unknown candidates \mathbf{x}' are generated from current unknowns \mathbf{x}
 152 by adding perturbation based on a proposal distribution (e.g., uniform or normal distribution).

153 Then, an acceptance probability α_{MH} is calculated as a ratio of the posterior PDFs when proposal
 154 PDFs $q(\mathbf{x}' | \mathbf{x})$ and $q(\mathbf{x} | \mathbf{x}')$ are symmetric [e.g., Fukuda & Johnson, 2008; Kubo et al., 2016]:

$$\alpha_{MH}(\mathbf{x}' | \mathbf{x}) = \min \left[1, \frac{p(\mathbf{x}' | \mathbf{d})}{p(\mathbf{x} | \mathbf{d})} \times \frac{q(\mathbf{x} | \mathbf{x}')}{q(\mathbf{x}' | \mathbf{x})} \right] \propto \min \left[1, \frac{p(\mathbf{x}' | \mathbf{d})}{p(\mathbf{x} | \mathbf{d})} \right]. \quad (7)$$

155 If $\alpha_{MH} > u$ (u is a random number generated from a uniform distribution with a range between 0
 156 and 1), the candidates are accepted. The unknown values are sampled during iterative updates of
 157 the unknowns based on the above process; the ensemble of the sampled unknown values
 158 demonstrates the estimates of the unknowns following their posterior PDFs.

159 For the rj-MCMC approach, an extended form of the acceptance probability in the MH
 160 algorithm has been generally utilized, which was implemented as the Metropolis-Hasting-Green
 161 (MHG) algorithm [Green, 1995; 2003]. The acceptance probability in the MHG algorithm is
 162 written as

$$\alpha_{MHG}(\mathbf{x}' | \mathbf{x}) = \min \left[1, \frac{p(\mathbf{x}' | \mathbf{d})}{p(\mathbf{x} | \mathbf{d})} \times \frac{q(\mathbf{x} | \mathbf{x}')}{q(\mathbf{x}' | \mathbf{x})} \times |\mathbf{J}| \right] \quad (8)$$

163 where \mathbf{J} is the Jacobian for the transformation from \mathbf{x} to \mathbf{x}' , which evaluates the scale changes
 164 due to a dimensional jump between \mathbf{x} and \mathbf{x}' . However, we can simply consider $|\mathbf{J}| = 1$ when the
 165 transformed dimension is less than one, such as in a case of the birth/death rj-MCMC method
 166 [e.g., Denison et al., 2002; Bodin & Sambridge, 2009]. In this study, we employed the
 167 birth/death rj-MCMC method. The details of the birth/death rj-MCMC method are denoted in
 168 Section 2-4. Thus, considering Equation (6), the acceptance probability in this study can be
 169 expressed as following:

$$\begin{aligned} \alpha(\mathbf{x}' | \mathbf{x}) &= \min[1, (\mathbf{prior\ ratio}) \times (\mathbf{likelihood\ ratio}) \times (\mathbf{proposal\ ratio})] \quad (9) \\ &= \min \left[1, \frac{p(\mathbf{x}')}{p(\mathbf{x})} \times \frac{p(\mathbf{d} | \mathbf{x}')}{p(\mathbf{d} | \mathbf{x})} \times \frac{q(\mathbf{x} | \mathbf{x}')}{q(\mathbf{x}' | \mathbf{x})} \right]. \end{aligned}$$

170 Like the ordinary MCMC, the unknowns are updated based on the acceptance probability
 171 and are sampled. The practical implementation of the dimensional jump and of the unknowns'
 172 update is denoted later.

173

174 2.3 Parameterization of unknowns

175 We introduced a set of the Voronoi nuclei to discretize a 2-dimensional fault plane as
 176 shown in Figure 1. The fault plane is covered by sub-faults (black rectangles). Each sub-fault
 177 was classified by distance from the Voronoi nuclei (red circles); this classification demonstrated
 178 the Voronoi cells (colors of sub-faults). The Voronoi nuclei are generated from a nucleus grid
 179 (gray dots). The total number of nucleus grid points is defined as K^{grid} . Using the Voronoi
 180 partition, the unknowns expressing fault slip distributions are defined as the combination of
 181 locations of the Voronoi nuclei \mathbf{c} and slips for individual cells $\bar{\mathbf{s}}$. Note that the slips $\bar{\mathbf{s}}$ are defined
 182 as a partitioned form of \mathbf{s} . Defining the number of the Voronoi nuclei for the j th fault-slip
 183 component is K_j , the unknown vector for the locations of the Voronoi nuclei \mathbf{c} can be written as

$$\mathbf{c} = \begin{pmatrix} \mathbf{c}_1 \\ \vdots \\ \mathbf{c}_j \\ \vdots \\ \mathbf{c}_{K_j} \end{pmatrix} = \begin{pmatrix} c_{1_1} \\ \vdots \\ c_{j_1} \\ \vdots \\ c_{K_j} \end{pmatrix}. \quad (10)$$

184 Note that each nucleus location c_{k_j} denotes a locational number of the nucleus grid; the
 185 locational number is assigned for each point of the nucleus grid in advance. The unknown vector
 186 for the slips $\bar{\mathbf{s}}$ can be written as

$$\bar{\mathbf{s}} = \begin{pmatrix} \bar{\mathbf{s}}_1 \\ \vdots \\ \bar{\mathbf{s}}_j \\ \vdots \\ \bar{\mathbf{s}}_{K_j} \end{pmatrix} = \begin{pmatrix} \bar{s}_{1_1} \\ \vdots \\ \bar{s}_{j_1} \\ \vdots \\ \bar{s}_{K_j} \end{pmatrix}. \quad (11)$$

187 Besides the unknowns expressing fault slip distributions, the number of the Voronoi
 188 nuclei and the weighting parameters also account for unknowns. Defining the number of the
 189 Voronoi nuclei for the j th fault-slip component is K_j , the unknown vector for number of the
 190 Voronoi nuclei is expressed as $\mathbf{k} = (K_1, \dots, K_j)$. Furthermore, the unknown vector for the
 191 weighting parameters is defined as $\mathbf{h} = (A_1, \dots, A_l)$. Thus, the unknown vector can be finally
 192 written as

$$\mathbf{x} = \begin{pmatrix} \mathbf{k} \\ \mathbf{h} \\ \mathbf{c} \\ \bar{\mathbf{s}} \end{pmatrix}. \quad (12)$$

194 2.4 Birth/death rj-MCMC algorithm

195 We summarized our birth/death rj-MCMC algorithm as a flowchart in Figure S2. Based
 196 on Bodin and Sambridge [2009] and Galetti and Curtis [2018], we iteratively optimized the
 197 unknowns from initial values by following three steps: (1) “slip update” updating the slip amount
 198 for a randomly chosen Voronoi cell \bar{s}_{k_j} ; (2) “weight update” updating the weighting parameters
 199 \mathbf{h} ; (3) “Voronoi partition update” updating the number of the Voronoi nuclei \mathbf{k} , the locations of
 200 the Voronoi nuclei \mathbf{c} , and the corresponding slip $\bar{\mathbf{s}}$.

201 In the step (1), we randomly chose the k th Voronoi cell of the j th fault-slip component
 202 with the slip of \bar{s}_{k_j} . According to Bodin and Sambridge [2009], we generated a new candidate of
 203 the slip parameter \bar{s}'_{k_j} as following:

$$\bar{s}'_{k_j} = \bar{s}_{k_j} + v\sigma_{\text{slip}} \quad (13)$$

204 where v is a random coefficient derived from a normal distribution $N(0,1)$ and σ_{slip} is a constant
 205 denoting the standard deviation of the proposal PDF for the slip. This step is same with the
 206 ordinary MH algorithm and does not involve a dimensional jump.

207 In the step (2), we generated a new candidate of the weighting parameters \mathbf{h}' as

$$\mathbf{h}' = \mathbf{h} + \sigma_{\text{scale}} \mathbf{v}, \quad (14)$$

208 where \mathbf{v} is a random coefficient vector (I dimensions) derived from a normal distribution $N(0,1)$
 209 and σ_{scale} is a constant denoting the standard deviation of the proposal PDF for the weighting
 210 parameters. This step is also same the ordinary MH algorithm and does not involve a
 211 dimensional jump.

212 We implemented the birth/death algorithm in step (3). According to Bodin and
 213 Sambridge [2009], we performed this step only at every odd iteration loop. Step (3) branches
 214 into three actions: (a) “birth” action that adds a new nucleus is added, (b) “death” action that
 215 chooses one nucleus randomly from the existing nuclei to eliminate, (c) “move” action that
 216 chooses the location of one nucleus randomly from the existing nuclei to relocate. In step (3), we
 217 randomly chose one of the actions with equal probability. The unknowns are updated without the
 218 dimensional jump in the move action, while they are updated with the dimensional jump in the
 219 birth and death actions. We produced a new candidate of the unknowns for each action, and
 220 evaluated the candidates using the acceptance probability. The acceptance ratio is calculated

221 based on the formulation of Bodin and Sambridge [2009] and Galetti and Curtis [2018]. The
 222 details of the acceptance probability are written in Text S1.

223 In the birth action, we randomly chose a target fault-slip component from J components.
 224 Then, we randomly added one nucleus for the target j th fault-slip component from the K^{grid} grid
 225 points except the currently existing nuclei listed in \mathbf{c}_j . According to this action, the total number
 226 of the nuclei for the j th fault-slip component was increased by 1 as $K'_j = K_j + 1$. Then, the
 227 locations of the nuclei were reformed as

$$\mathbf{c}'_j = \begin{pmatrix} \mathbf{c}_j \\ c'_{K'_j} \end{pmatrix} \quad (15)$$

228 where $c'_{K'_j}$ is the locational number of the new nucleus. The slips of the nuclei were also
 229 reformed as

$$\bar{\mathbf{s}}'_{k_j} = \begin{pmatrix} \bar{\mathbf{s}}_j \\ \bar{s}'_{K'_j} \end{pmatrix} \quad (16)$$

230 where the slip of the new cell $\bar{s}'_{K'_j}$ was derived from the slip of the existing cell where the new
 231 nucleus was introduced with perturbation. If the nucleus controlling the existing cell is defined as
 232 k_j^c , the slip at the new cell $\bar{s}'_{K'_j}$ can be written as

$$\bar{s}'_{K'_j} = \bar{s}_{k_j^c} + \nu\sigma_{\text{jump}} \quad (17)$$

233 where σ_{jump} is a constant denoting the standard deviation of the proposal PDF for the slip due to
 234 the dimensional jump.

235 In the death action, we randomly chose a target fault-slip component from J components.
 236 Then, we randomly eliminated one nucleus of the target j th fault-slip component from the
 237 currently existing nuclei. According to this action, the total number of the nuclei for the j th fault-
 238 slip component was decreased by 1 as $K'_j = K_j - 1$. Then, the locations of the nuclei and the
 239 slips of the cells were reformed just excluding the corresponding fault-slip component.

240 In the move action, we randomly chose a target fault-slip component from J components.
 241 Then, we randomly chose one nucleus from the currently existing nuclei of the target j th fault-
 242 slip component, and relocated its point to another nucleus randomly chosen from the grid points
 243 within specific distances from the original nucleus; the specific distances are defined by $r_{\text{move}}^{\text{str}}$
 244 and $r_{\text{move}}^{\text{dip}}$ in the strike and dip directions, respectively. In this action, the total number of the

245 nuclei and the slips were kept $\mathbf{k}' = \mathbf{k}$ and $\overline{\mathbf{s}}' = \overline{\mathbf{s}}$. For the locations of the nuclei \mathbf{c}'_j , they were
 246 kept from the existing locations \mathbf{c}_j except the chosen nucleus.

247 After these three steps, we sampled the unknowns with a specific loop interval of the
 248 loops if the number of the iteration loops n was over the number of burn-in loops $N_{\text{burn-in}}$. To
 249 sample well-converged unknowns, the unknowns during the burn-in loops were discarded. As
 250 not all unknowns were updated in a single iteration loop, we only sampled the unknowns with a
 251 specific loop interval. In this study, we sampled every 100th iteration loop based on Bodin and
 252 Sambridge [2009]. Finally, we sampled the unknowns until n reached N_{all} .

253 In this study, we performed the above rj-MCMC algorithm for L multi-chains with
 254 (multi-chains approach); we assigned different initial values of \mathbf{x}^{ini} for each chain and sampled
 255 the unknowns parallelly from the multi-chains. As noted by Brooks et al. [2011] and Somogyvári
 256 and Reich [2019], the multi-chains approach is useful to reduce computational times by parallel
 257 computing compared with a long single-chain approach. Furthermore, calculating the ensemble
 258 of the samples from the multiple chains, we can obtain robust solutions regardless of influence
 259 on the initial values. As the length of each chain in the multi-chains approach is shorter than the
 260 long single-chain approach, the multi-chains approach is relatively sensitive to the length of the
 261 burn-in loops (i.e., degree of convergence). Thus, a parallel tempering technique has been often
 262 employed to accelerate the convergence [e.g., Sambridge, 2013; Dettmer et al., 2014]. However,
 263 this technique has difficulty in properly assigning the number of parallel replicas and their
 264 potential temperatures. Thus, we calculated solutions for the slip by a conventional ABIC-LSM,
 265 \mathbf{s}^{LSM} , and produced L sets of the initial partitioned solutions $\overline{\mathbf{s}}^{\text{ini}}$ from \mathbf{s}^{LSM} assuming various
 266 distributions of initial Voronoi nuclei ($\mathbf{c}^{\text{ini}}, \mathbf{k}^{\text{ini}}$). Because \mathbf{s}^{LSM} can be regarded as well-
 267 converged initial values, we can perform the multi-chains approach effectively and simply
 268 without the parallel tempering technique. \mathbf{s}^{LSM} was estimated following Yabuki and Matsu'ura
 269 [1992], and the details of this estimation method are written in Text S2.

270 In this study, we uniformly assigned the following configuration of rj-MCMC: $L =$
 271 2000, $N_{\text{burn-in}} = 1000000$, $N_{\text{all}} = 1250000$, and $K_j^{\text{ini}} = 20$ ($j = 1, \dots, J$). Considering that the
 272 unknowns are sampled every 100th iteration loop, we fully obtained 5×10^6 samples from the
 273 multi-chains. Note that the initial distributions of the Voronoi nuclei \mathbf{c}^{ini} were randomly
 274 generated from the nucleus grid following the number of the initial Voronoi nuclei \mathbf{k}^{ini} .

275 Moreover, we basically assigned the minimum and maximum numbers of the Voronoi nuclei for
276 each fault-slip component as $K_j^{\min} = 5$ and $K_j^{\max} = 50$ ($j = 1, \dots, J$), respectively, which are
277 used in Equation (S2) and (S3) of Text S1. We also assigned the minimum and maximum values
278 of the weighting parameters as $\Lambda_i^{\min} = -10$ and $\Lambda_i^{\max} = 10$ ($i = 1, \dots, I$), respectively for the
279 all estimations, which are used in Equation (S8) and (S9) of Text S1.

280

281 **3 Synthetic tests**

282 **3.1 Model configuration**

283 Here, we investigated performance of the trans-dimensional geodetic inversion using the
284 rj-MCMC technique through synthetic tests assuming fault slips in a subduction zone. A plate
285 interface with uniform dip of 15° in a semi-infinite space was assumed as shown in Figure S2.
286 The fault domain was approximately 500 km (along strike) \times 310 km (along dip), and its upper
287 limit reached to the surface corresponding to the trench. We then laid sub-faults with size of
288 approximately 20 km \times 20.7 km on the plate interface, and total number of the sub-faults is 375.
289 We located randomly distributed 150 synthetic observational sites within the a range of 200–400
290 km from the trench as onshore GNSS sites. Moreover, we located synthetic observational sites
291 within the a range of 0–200 km from the trench as offshore GNSS-A sites. Three patterns of the
292 offshore observational site distribution were assumed: (1) no site, (2) five randomly distributed
293 sites, and (3) twenty-five randomly distributed sites. We calculated synthetic displacements at
294 these sites due to a given fault slip distribution, and then we obtained synthetic observational
295 data by adding observational errors.

296

297 **3.2 Synthetic test 1: response to smooth coseismic slip**

298 In the synthetic test, a smooth coseismic slip distribution with maximum slip of ~ 700 cm
299 was provided to calculate synthetic observational data for three site patterns (“Target” column of
300 Figure 2). In this test, we assumed an elastic media [Okada, 1992], and we calculated the Green
301 functions in the directions of rake = 45° and of rake = 135° (i.e., the fault-slip components were

302 defined as $J = 2$, and total number of the unknowns for slip is $375 \times 2 = 750$). Then, imposing
 303 non-negative constraints on the slip, we restricted the slip rake within the range from 45° to 135°
 304 in the same manner as Miyazaki et al. [2011]. We assigned the minimum and maximum slips as
 305 $\bar{s}_j^{\min} = 0$ [cm] and $\bar{s}_j^{\max} = 3000$ [cm] ($j = 1, 2$), respectively. The observational errors were
 306 added as the Gaussian noises of

$$(\sigma_{\text{onhor}}, \sigma_{\text{onver}}, \sigma_{\text{offhor}}, \sigma_{\text{offver}}) = (1, 2, 3, 6) \text{ [cm]} \quad (18)$$

307 indicating standard deviations for horizontal components of the onshore sites, vertical component
 308 of the onshore sites, horizontal components of the offshore sites, and vertical component of the
 309 offshore sites, respectively. The standard deviations for the offshore sites are given following the
 310 case of the 2005 Miyagi-oki earthquake shown in Sato et al. [2013]. We provided single
 311 weighting parameter uniformly scaling all data for simplicity (i.e., $I = 1$). Because we assigned a
 312 diagonal matrix for the initial observational covariance matrix $\mathbf{E}_1^{\text{ini}}$ following Equation (18), the
 313 weighting parameter should be zero (i.e., the weight matrix should be on the initial condition:
 314 $\mathbf{W}_1 = 10^0 \mathbf{W}_1^{\text{ini}}$).

315 From the synthetic observational data, we estimated fault-slip distributions by the ABIC-
 316 LSM and the rj-MCMC method, which are shown in “ABIC-LSM” and “Rj-MCMC” columns of
 317 Figure 2, respectively. Note that the “Error” column of ABIC-LSM demonstrates standard
 318 deviations calculated from diagonal components of the covariance matrix. For the rj-MCMC
 319 results, we used two methods to express a slip distribution: mean and median of the samples.
 320 Moreover, we calculated the standard deviation of the samples (“SD” column) and the
 321 normalized interquartile range (NIQR) of samples (“NIQR” column) as estimation errors. The
 322 synthetic (without the observational errors), observational (with the observational errors), and
 323 calculated (from the estimated model) displacements are shown in Figure 2 as magenta, black,
 324 and blue vectors.

325 Figure 3c shows histograms of the unknowns for site pattern 2. The histograms
 326 demonstrated that total number of the unknowns for slip was reduced from 750 to ~ 10 – 12 by the
 327 Voronoi partition and that the weighting parameter was properly kept at zero. For the slip
 328 unknowns, the histograms at three sub-faults shown in Figure 3a are demonstrated for example.

329 The slip at the m th sub-fault was calculated as $s_m = \sqrt{s_{m_1}^2 + s_{m_2}^2}$ when defining s_{m_j} as the slip
 330 at the m th sub-fault in the j th fault-slip component. Figures S3 and S4 also show histograms for

331 the unknowns in the cases for site patterns 1 and 3, respectively. The histograms at the sub-fault
332 A are similar to the Gaussian distribution in all cases of the site patterns, whereas we can find the
333 histograms with multiple peaks or those with a biased distribution at the sub-fault B and at sub-
334 fault C, respectively, in the cases of the site patterns 1–2. These histograms following non-
335 Gaussian distributions are considered to be caused by the lack of the offshore observational sites
336 as the slip amounts at these sub-fault were not well constrained. Although we showed the
337 standard deviation of the samples to visualize estimation errors (“SD” in Figure 2), the standard
338 deviation of the samples potentially assumes a Gaussian distribution of the samples. Thus, to
339 visualize the estimation error following a non-Gaussian distribution, we also showed the map of
340 NIQR. If the observational error follows a Gaussian distribution, NIQR corresponds to SD;
341 therefore, we can roughly interpret that the estimation errors are close to Gaussian distributions
342 when the mean and the standard deviation resemble the median and the median and the NIQR,
343 respectively. Furthermore, to visualize details of the PDFs for the slip such as due to multiple
344 peaks or a biased distribution, we calculated differences of the percentiles (subtracting 50th
345 percentile from 5th, 25th, 75th, and 95th percentiles) in Figures 3b, S3b, and S4b. For example,
346 we considered that a PDF of the slip amount shows a biased distribution with a long slope to the
347 high slip; 5th and 25th percentile differences demonstrate small absolute values, while 75th and
348 95th percentile differences demonstrate large absolute values such as sub-fault C in the cases of
349 the site patterns 1–2.

350 The target slip distributions were well reproduced both by the ABIC-LSM and by the rj-
351 MCMC method for the cases of the site patterns 2 and 3. Furthermore, both of the ABIC-LSM
352 and the rj-MCMC method underestimated the maximum slip for the case of the slip pattern 1
353 because no offshore site was employed. However, the estimated slip distribution of ABIC-LSM
354 was obviously over-smoothed in the along-strike direction. By contrast, the rj-MCMC method
355 reduced such over-smoothing in the along-strike direction. It is considered that this effect was
356 caused by a sparse modeling behavior of the rj-MCMC method. Furthermore, among all site
357 patterns, the rj-MCMC method successfully reduced spotting artificial slips appearing in the all
358 slip distribution estimated by the ABIC-LSM. This effect is also considered to be provided as the
359 sparse modeling behavior of the rj-MCMC method.

360 For all slip pattern cases, the slip distributions estimated by the rj-MCMC method
361 generally show large slip near the trench compared with those estimated by the ABIC-LSM. This

362 is because the rj-MCMC method sampled a low probability of large slips near the trench as
363 demonstrated by the histograms of sub-fault C and the 95th percentile difference (Figures 3, S3,
364 and S4). Because spatial resolution near the trench was low due to the lack of the observational
365 sites, large coseismic slip there was considered to occur with low probability as modeled by the
366 rj-MCMC. However, ABIC-LSM cannot properly consider such a low probability phenomenon
367 in the solutions because Gaussian distribution of the solutions was assumed.

368 We showed two models for the results of the rj-MCMC method: the mean and median
369 models as shown in Figure 2. Their slip distributions were quite similar except the region near
370 the trench where the large slip was considered to occur with the low probability. Because the
371 median is generally smaller than the mean when the biased PDF with a long slope to the high slip
372 (e.g., the histogram of sub-fault C in Figure 3c), the seismic moment of the median model is
373 smaller than that of the mean model; for example, in the case of the site pattern 1, the moment
374 magnitude of the median model is M_w 8.18, while that of the mean model is M_w 8.24. We
375 evaluated the mean model as a better representative model because the seismic moments of the
376 mean model were generally close to the seismic moment of the target model. However, the
377 median model and its corresponding estimation error (NIQR) provided useful information to
378 know degree how the unknowns for the slip follow the Gaussian distribution or not as indicated
379 above.

380

381 3.3 Synthetic test 2: response to sharp coseismic slip

382 In this synthetic test, a sharp coseismic slip distribution with maximum slip of
383 approximately 1000 cm was provided to calculate synthetic observational data for the three site
384 patterns as in synthetic test 1, and then we estimated slip distributions by the ABIC-LSM and the
385 rj-MCMC method as shown in Figure 4. Considering the elasticity of plates, deformation due to
386 fault locking at asperities should be continuous; therefore, coseismic slip should be rather
387 continuous (i.e., edge of fault slip distribution tends to be smooth) [Herman et al., 2018]. Thus,
388 the target slip distribution in this synthetic test is slightly unrealistic but effective to evaluate the
389 performance of the inversion techniques.

390 The ABIC-LSM model failed to reproduce the target slip distribution in any cases of the
391 site patterns (Figure 4), because the assumption of the smoothing was unsuitable to model such a

392 sharp distribution. To forcibly reproduce sharp edges of the slip patch, the ABIC-LSM provided
 393 a weak smoothing constraint; hence, the estimated slip distributions were highly dependent on
 394 location of the observational sites especially as shown in site pattern 3. In contrast, the rj-MCMC
 395 method successfully reproduced the target slip distribution, because the Voronoi partition was
 396 potentially suitable for producing sharp edges. Summarising the results of the synthetic tests 1
 397 and 2, the rj-MCMC method can flexibly represent a fault slip distribution regardless of the site
 398 distribution and of roughness on the target slip distribution.

399

400 3.4 Synthetic test 3: behavior of the weighting parameters

401 In this synthetic test, performance of the weighting parameters was investigated by
 402 applying incorrect initial observational errors. We provided the smooth coseismic slip
 403 distribution for the target slip distribution as employed in synthetic test 1 and performed the rj-
 404 MCMC inversion under the same conditions as synthetic test 1 except the observational errors.
 405 Note that we performed the inversion only for the data assuming the site pattern 3. Here, dual
 406 weighting parameters were employed (i.e., $I = 2$): the weighting parameter for the onshore
 407 observational data ($i = 1$) and that for the offshore observational data ($i = 2$), regardless of
 408 distinction between the horizontal and vertical components. Then, two types of the observational
 409 error conditions were investigated; one assumed that the true observational errors, which were
 410 added to the synthetic observational data, were smaller than the initial observational errors (the
 411 smaller error case); and the other assumed the true observational errors were larger than the
 412 initial observational errors (the larger error case). In the former case, the true observational errors
 413 were added as the Gaussian noises of

$$(\sigma_{\text{on}_{\text{hor}}}, \sigma_{\text{on}_{\text{ver}}}, \sigma_{\text{off}_{\text{hor}}}, \sigma_{\text{off}_{\text{ver}}}) = (1, 2, 3, 6) \text{ [cm]}, \quad (19)$$

414 like synthetic test 1, while the initial observational errors were given as

$$(\sigma_{\text{on}_{\text{hor}}}^{\text{ini}}, \sigma_{\text{on}_{\text{ver}}}^{\text{ini}}, \sigma_{\text{off}_{\text{hor}}}^{\text{ini}}, \sigma_{\text{off}_{\text{ver}}}^{\text{ini}}) = (1, 2, 30, 60) \text{ [cm]}. \quad (20)$$

415 In the later case, the true observational errors were added as the Gaussian noises of

$$(\sigma_{\text{on}_{\text{hor}}}, \sigma_{\text{on}_{\text{ver}}}, \sigma_{\text{off}_{\text{hor}}}, \sigma_{\text{off}_{\text{ver}}}) = (1, 2, 30, 60) \text{ [cm]} \quad (21)$$

416 while the initial observational errors were given as

$$(\sigma_{\text{on}_{\text{hor}}}^{\text{ini}}, \sigma_{\text{on}_{\text{ver}}}^{\text{ini}}, \sigma_{\text{off}_{\text{hor}}}^{\text{ini}}, \sigma_{\text{off}_{\text{ver}}}^{\text{ini}}) = (1, 2, 3, 6) \text{ [cm]}. \quad (22)$$

417 For comparison, we also estimated fault slip distributions by the rj-MCMC method assuming the
 418 single weighting parameter in the same manner as synthetic test 1.

419 The upper panels of Figure 5 show the results for the smaller error case. When assuming
 420 the single weighting parameter, the estimated slip distribution and its standard deviation are
 421 similar to those of the synthetic test 1 for the site pattern 1. This similarity suggested that the
 422 offshore observational data were almost ignored because of the employed large initial
 423 observational errors (Equation 20). When assuming the dual weighting parameters, the estimated
 424 slip distribution and its standard deviation are similar to those of synthetic test 1 for site pattern 3
 425 (Figure 2). This suggests that the weighting parameter for the offshore observational data
 426 increased the weights of the offshore observational data. Actually, the observational errors
 427 adjusted by the weighting parameters were given as

$$\begin{aligned}
 & (\hat{\sigma}_{\text{onhor}}, \hat{\sigma}_{\text{onver}}, \hat{\sigma}_{\text{offhor}}, \hat{\sigma}_{\text{offver}}) & (23) \\
 & = \left(10^{-\frac{\Lambda_1}{2}} \sigma_{\text{onhor}}^{\text{ini}}, 10^{-\frac{\Lambda_1}{2}} \sigma_{\text{onver}}^{\text{ini}}, 10^{-\frac{\Lambda_2}{2}} \sigma_{\text{offhor}}^{\text{ini}}, 10^{-\frac{\Lambda_2}{2}} \sigma_{\text{offver}}^{\text{ini}} \right) \\
 & = (1.01, 2.03, 4.36, 8.72) \text{ [cm]}.
 \end{aligned}$$

428 The weighting parameters used in Equation (23) were calculated as the mean values of the rj-
 429 MCMC samples. The histograms of the weighting parameters are shown in Figure S5. Because
 430 the adjusted observational errors for the offshore data were rather larger than the true
 431 observational errors (Equation 19), the estimated slip distribution was also smoother than that of
 432 the synthetic test 1 for site pattern 3.

433 The lower panels of Figure 5 show the results for the larger error case. When assuming
 434 the single weighting parameter, the estimated slip distribution was extremely rough. In this
 435 result, the offshore observational data were over-fitted because of the employed small initial
 436 observational errors (Equation 22). By contrast, when assuming the dual weighting parameters,
 437 the estimated slip distribution reproduced the target smooth distribution by degrading the weights
 438 of the offshore observational data by the weighting parameters. The observational errors adjusted
 439 by the mean weighting parameters were given as

$$\begin{aligned}
 & (\hat{\sigma}_{\text{onhor}}, \hat{\sigma}_{\text{onver}}, \hat{\sigma}_{\text{offhor}}, \hat{\sigma}_{\text{offver}}) & (24) \\
 & = \left(10^{-\frac{\Lambda_1}{2}} \sigma_{\text{onhor}}^{\text{ini}}, 10^{-\frac{\Lambda_1}{2}} \sigma_{\text{onver}}^{\text{ini}}, 10^{-\frac{\Lambda_2}{2}} \sigma_{\text{offhor}}^{\text{ini}}, 10^{-\frac{\Lambda_2}{2}} \sigma_{\text{offver}}^{\text{ini}} \right)
 \end{aligned}$$

$$= (1.01, 2.03, 31.77, 63.54) \text{ [cm]}.$$

440 which are well fitted to the true observational errors (Equation 21). The histograms of the
441 weighting parameters are shown in Figure S6 as well as the histograms of the other unknowns.

442 From the above results, the weighting parameters properly adjusted the initial
443 observational errors by the data-driven approach. Considering that the initial large observational
444 errors provided a little smooth slip distribution even using the weighting parameter (the smaller
445 error case), we would assign rather small initial observational errors and adjust them by the
446 weighting parameters in a practical use of the rj-MCMC method as shown later in Section 4.

447

448 3.5 Synthetic test 4: coupling estimation

449 In this synthetic test, we provided synthetic negative fault slips assuming annual inter-
450 seismic coupling (Figure 6). An elastic media [Okada, 1992] was assumed, and we calculated the
451 Green functions in the direction of rake=90° alone (i.e., $J = 1$). The minimum and maximum slip
452 rates were assigned as $\bar{s}_1^{\min} = -83.5$ [mm/yr] and $\bar{s}_1^{\max} = 500$ [mm/yr], respectively. The
453 minimum slip rate was provided as a subducting rate in the off-Tohoku region, Japan. The
454 observational errors were added as the Gaussian noises of

$$(\sigma_{\text{GNSS}_{\text{hor}}}, \sigma_{\text{GNSS}_{\text{ver}}}, \sigma_{\text{GNSS-A}_{\text{hor}}}) = (1.5, 3, 5) \text{ [mm/yr]}. \quad (25)$$

455 We ignored the vertical component of the offshore sites because the GNSS-A measurement has
456 too large observational errors to discuss small coupling conditions. The standard deviation for
457 the horizontal components of the offshore sites was given following the case of interseismic
458 displacement rates for the Nankai and Tohoku regions shown in Sato et al. [2013] and Yokota et
459 al. [2016]. The initial observational errors were given following the true observational errors
460 (Equation 25), and the single weighting parameter was given ($I = 1$). The aim of this test was to
461 assess performance of the rj-MCMC method for the coupling estimation and for difficult
462 inversion conditions compared with the coseismic slip cases: multiple peaks of fault slip
463 (“Target” of Figure 6) and low signal-noise ratio.

464 Figure 6 shows the inversion results estimated by the ABIC-LSM and the rj-MCMC
465 method for site patterns 1 and 3. In the both of the site patterns, the ABIC-LSM provided fairly
466 smooth coupling distributions because the difficult inversion conditions required strong

467 smoothing constraints. The rj-MCMC method also provided smooth coupling distributions for
468 site pattern 1 due to the low spatial resolution in the offshore area. However, down-dip limits of
469 the coupling distribution estimated by the rj-MCMC method were substantially constrained
470 compared with those estimated by the ABIC-LSM. This indicated that flexibility of the spatial
471 partition by the rj-MCMC method enables smooth edge expression of the up-dip limits (due to
472 low spatial resolution) and relatively sharp edge expression of the down-dip limits (due to
473 relatively high spatial resolution). The rj-MCMC method obviously demonstrated better
474 performance for site pattern 3; peaks of the coupling distribution in the northern and middle
475 regions were clearly obtained. Thus, the rj-MCMC method has superior ability to avoid the over-
476 smoothing compared with the ABIC-LSM. Meanwhile, the southern peak of the coupling could
477 not be imaged even by the rj-MCMC method because of its narrow spatial extent and insufficient
478 deployment of the offshore observational sites.

479 Figure 6 shows that distributions of the standard deviation are obviously different from
480 that of NIQR in both of the site patterns. This suggests the observational errors did not generally
481 follow Gaussian distributions. Figures S7 and S8 show percentile differences and histograms of
482 the unknowns for cases of site patterns 1 and 3, respectively. Figure S7 clearly shows positive
483 slip with low probability in the northern area near the trench, and also indicates low spatial
484 resolution there. Figure S8 shows multiple histogram peaks, especially the histogram for the slip
485 at sub-fault D (in the northern area near the trench). For the sub-fault D, we can interpret that
486 both possibilities of strong coupling and zero coupling are considered at the same level taking
487 into account the insufficient spatial resolution. Thus, the rj-MCMC method is useful to assess
488 how risk of the coupling occurs at each sub-fault from the histogram or the percentile difference,
489 which cannot be expressed by the conventional ABIC-LSM.

490

491 3.6 Synthetic test 5: viscoelastic inversion

492 In this synthetic test, we provided synthetic coseismic slip distribution (period 1) and
493 postseismic slip distributions with three time windows (periods 2–4; the duration for each period
494 was set as one year). We assumed a two-layered viscoelastic media [Fukahata & Matsu'ura,
495 2004] in the same manner as Tomita et al. [2020]: viscosity in the lower media of 1.5×10^{19} Pa
496 s, thickness of the upper media of 50 km, rigidities in the upper and lower media of 40 GPa and

497 67 GPa, densities in the upper and lower media of 2800 kg/m^3 and 3300 kg/m^3 , and Poisson's
 498 ratios in the upper and lower media of 0.25 and 0.27, respectively. We then calculated the
 499 viscoelastic Green functions in the directions of rake= 45° and rake= 135° for the coseismic slip
 500 and in the direction of rake= 90° alone for the postseismic slip (i.e., $J = 5$). The minimum and
 501 maximum slips for the coseismic period were assigned as $\bar{s}_j^{\min} = 0 \text{ [cm]}$ and $\bar{s}_j^{\max} = 6000 \text{ [cm]}$
 502 ($j = 1, 2$), respectively, and those for the postseismic period were assigned as $\bar{s}_j^{\min} =$
 503 -8.35 [cm] and $\bar{s}_j^{\max} = 500 \text{ [cm]}$ ($j = 3, \dots, 5$), respectively. Based on the 2011 Tohoku-oki
 504 earthquake, we assumed that the offshore sites were installed in the postseismic period (here, the
 505 period 3). The observational errors for the coseismic period were added as the Gaussian noises of

$$(\sigma_{\text{GNSS}_{\text{hor}}}, \sigma_{\text{GNSS}_{\text{ver}}}) = (1, 2) \text{ [cm]}. \quad (26)$$

506 The observational errors for the postseismic period were added as the Gaussian noises of

$$(\sigma_{\text{GNSS}_{\text{hor}}}, \sigma_{\text{GNSS}_{\text{ver}}}, \sigma_{\text{GNSS-A}_{\text{hor}}}, \sigma_{\text{GNSS-A}_{\text{ver}}}) = (0.5, 1, 2, 4) \text{ [cm/yr]}. \quad (27)$$

507 The standard deviations of the offshore sites were given following the postseismic displacements
 508 after the 2011 Tohoku-oki earthquake shown in Watanabe et al. [2014], Tomita et al. [2017], and
 509 Yokota et al. [2018]. The initial observational errors were given following the true observational
 510 errors, and the four weighting parameters were given to individual time-window ($I = 4$). The
 511 aim of this test was to assess performance of the rj-MCMC method for estimation of
 512 spatiotemporal evolution of fault slip, which basically requires many hyper-parameters
 513 constraining both spatial space and temporal space [e.g., Yoshioka et al., 2015]. In this case, we
 514 individually deployed Voronoi nuclei for each time-window and estimated fault slip distributions
 515 considering viscoelastic responses without any external constraints. Although we can introduce
 516 temporal smoothing constraints in our rj-MCMC method, we did not use the constraints for
 517 simplicity.

518 For comparison and obtaining initial values, we also performed the ABIC-LSM as well as
 519 the rj-MCMC method. In the rj-MCMC method, we simultaneously estimated the co- and post-
 520 seismic slip distributions based on the following observation equation for the viscoelastic
 521 inversion approach derived from Tomita et al. [2020]:

$$\begin{pmatrix} \mathbf{d}_1 \\ \mathbf{d}_2 \\ \mathbf{d}_3 \\ \mathbf{d}_4 \end{pmatrix} = \begin{pmatrix} \mathbf{G}_{1,1}^e & \mathbf{G}_{1,2}^e & \mathbf{0} & \cdots & \mathbf{0} \\ \mathbf{G}_{2,1}^v & \mathbf{G}_{2,2}^v & \mathbf{G}_{2,3}^e & \ddots & \vdots \\ \mathbf{G}_{3,1}^v & \mathbf{G}_{3,2}^v & \mathbf{G}_{3,3}^v & \mathbf{G}_{3,4}^e & \mathbf{0} \\ \mathbf{G}_{4,1}^v & \mathbf{G}_{4,2}^v & \mathbf{G}_{4,3}^v & \mathbf{G}_{4,4}^v & \mathbf{G}_{4,5}^e \end{pmatrix} \begin{pmatrix} \mathbf{s}_1 \\ \mathbf{s}_2 \\ \mathbf{s}_3 \\ \mathbf{s}_4 \\ \mathbf{s}_5 \end{pmatrix} + \begin{pmatrix} \mathbf{e}_1 \\ \mathbf{e}_2 \\ \mathbf{e}_3 \\ \mathbf{e}_4 \end{pmatrix}, \quad (28)$$

522 where \mathbf{G}^e and \mathbf{G}^v represent the elastic and viscous Green functions, respectively. However, in the
 523 ABIC-LSM, we estimated a fault slip distribution of each time-window step by step as similar
 524 with Lubis et al. [2013] to avoid difficulty in determining multiple hyper-parameters.

525 Figure 7 shows the target and the estimated slip distributions. The slip and error maps of
 526 the rj-MCMC method demonstrated mean and standard deviation of the samples, respectively.
 527 The rj-MCMC results well reproduced the target distributions as well as the results of the ABIC-
 528 LSM except the period 2 in which effective offshore observational sites were absent. Unlike the
 529 ABIC-LSM, the rj-MCMC method successfully reduced artificial negative postseismic slip.
 530 Although the smoothing constraint of the ABIC-LSM cannot prevent generation of spotting
 531 artificial slips, the rj-MCMC method can prevent it by unifying the sub-faults by the Voronoi
 532 partition. Thus, the rj-MCMC method is useful to model such spatiotemporal evolution of the
 533 fault slip without any constraints. Additionally, as with the other synthetic tests above, the
 534 estimation errors imaged precision of the solutions, which cannot be assessed by the ABIC-LSM.
 535 We also showed median model at percentile differences in Figure S9 to assess non-Gaussian
 536 errors.

537

538 3.7 Checkerboard resolution test

539 From the above synthetic tests, the estimation errors of the rj-MCMC method (standard
 540 deviation and NIQR) demonstrated good performance of imaging precision of the solutions for
 541 the fault slip; however, it is difficult to consider spatial resolution from the results. To evaluate
 542 spatial resolution, we conducted checkerboard resolution tests. As it is difficult to evaluate
 543 spatial resolution for the overall fault space by single checkerboard pattern, we conducted the
 544 checkerboard resolution test for various patterns in which checkerboard patches were slightly
 545 shifted (Figure S10). Here, we generated eighteen total checkerboard patterns. Note that
 546 observational noises, which were given to generate the synthetic observational data, followed the
 547 observational errors adjusted by the weighing parameter in the synthetic test 1. The upper limits

548 of the Voronoi nuclei are set as $K_j^{\max} = 50$ ($j = 1, 2$) in the checkerboard resolution tests. Figure
 549 8a shows an example of the inversion result for a single checkerboard pattern. The results for all
 550 checkerboard patterns are shown in Figure S10. For each checkerboard pattern, a patch with the
 551 size of $\sim 60 \times 60 \text{ km}^2$ and with the slip of $\sim 425 \text{ cm}$ was provided. The patch size and the slip
 552 amount for patch should be manually changed to conform with our target slip behavior by which
 553 we intend to assess sensitivity of the observational data to. To summarize the results, we
 554 introduced a new indicator called as the “reconstruction ratio”. The reconstruction ratio for a
 555 sub-fault m is written as follows:

$$RR_m = 100 - \frac{1}{\tilde{L}} \frac{\sum_{l=1}^L |\tilde{s}_{m,l}^{\text{cal}} - s_{m,l}^{\text{syn}}|}{s^{\text{syn}}} \times 100 [\%], \quad (29)$$

556 with $\tilde{s}_{m,l}^{\text{cal}} = \begin{cases} s_{m,l}^{\text{cal}} & \text{if } s_{m,l}^{\text{syn}} > 0 \\ 0 & \text{if } s_{m,l}^{\text{syn}} = 0 \end{cases}$,

557 where s^{syn} is the slip amount of the slip patch ($\sim 425 \text{ cm}$ in this case), and $s_{m,l}^{\text{cal}}$ and $s_{m,l}^{\text{syn}}$ are the
 558 estimated and the target slips at the sub-fault m for the pattern l , respectively. Moreover, L is the
 559 total number of the checkerboard patterns ($L = 18$), and \tilde{L} is the total number of the
 560 checkerboard pattern that provided the slip (non-zero slip) at the sub-fault m . As defined by $\tilde{s}_{m,l}^{\text{cal}}$,
 561 we only considered recovery at the sub-faults where synthetic slip was provided by the target slip
 562 distribution. Because we provided a set of normal and reverse checkerboard patterns (see the
 563 target distributions of 1 and 4 in Figure S10, for example), $\tilde{L} = L/2$. A map of the reconstruction
 564 ratio (Figure 8b) clearly demonstrated that high reconstruction ratios (corresponding to high
 565 spatial resolution) appeared roughly below the observational sites. A checkerboard resolution test
 566 has been often performed in ABIC-LSM approaches; however, it is difficult to assess intrinsic
 567 sensitivity of the observational data because the degree of recovery was quite influenced by
 568 strength of a smoothing constraint in ABIC-LSMs. If the smoothing constraint is optimized for a
 569 checkerboard slip distribution, it is not suitable for a practical slip distribution. Whereas, if the
 570 smoothing constraint is optimized for a practical slip distribution, it is not suitable for a
 571 checkerboard slip distribution. Meanwhile, as the smoothing constraint is not used in the rj-
 572 MCMC method, the checkerboard resolution tests through the rj-MCMC method are much
 573 effective to demonstrate sensitivity of the observational data.

574

575 4 Application to the 2011 Tohoku-oki earthquake

576 Here, we applied the rj-MCMC method to coseismic geodetic observational data
577 associated with the 2011 Tohoku-oki earthquake (March 11, 2011). We constructed 485 sub-
578 faults based on the plate interface model of Iwasaki et al. [2015]. As with synthetic test 1, an
579 elastic media [Okada, 1992] was assumed, and the Green functions in the directions of rake=45°
580 and of rake=135° were calculated ($J = 2$; total number of the unknowns for slip is $485 \times 2 =$
581 970). When calculating the Green functions for offshore sites (denoted later), we considered
582 seafloor depths by biasing the depths of the sub-faults along the plate interface in the same
583 manner as Inuma et al. [2012]. Minimum and maximum slips were assigned as $\bar{s}_j^{\min} = 0$ [m]
584 and $\bar{s}_j^{\max} = 100$ [m] ($j = 1,2$), respectively.

585 We employed the following types of the observational data: onshore GNSS (horizontal
586 and vertical), offshore GNSS-A (horizontal and vertical), and offshore OBP gauge (vertical)
587 data. The onshore GNSS data were differences between the daily coordinate solutions for the day
588 before the mainshock (March 10, 2011) and those for the day after the mainshock (March 12,
589 2011) at 370 GNSS sites maintained by the Geospatial Information Authority of Japan (GSI) and
590 Tohoku University, which were obtained by Tomita et al. [2020]. The offshore GNSS-A data
591 were provided by the Japan Coast Guard (six sites with horizontal and vertical components)
592 [Sato et al., 2011; Yokota et al., 2018] and Tohoku University (two sites with horizontal
593 component only) [Kido et al., 2011]. The offshore OBP data were provided by University of
594 Tokyo and Tohoku University (six sites) [Ito et al. 2011; Meade et al., 2011] as summarized by
595 Inuma et al. [2012]. The onshore GNSS and the offshore OBP data indicate almost pure
596 coseismic displacements, while the offshore GNSS-A data include not only coseismic
597 displacements but also early (~1 month) postseismic displacements [Kido et al., 2011; Sato et al.,
598 2011]. Then, as for the offshore GNSS-A data, it is unsuitable to assign instrumental
599 measurement errors as observational errors for the inversion analysis considering the
600 observational errors included not only instrumental measurement errors but also the modeling
601 errors of the early postseismic displacements. Thus, we adopted an approach providing rough
602 initial observational errors of the offshore GNSS-A data and then adjusting them by the
603 weighting parameters. The observational errors of the offshore GNSS-A data in the horizontal

604 and vertical components were quite different for both the instrumental measurement errors and
 605 the early postseismic displacements; hence, we provided three weighting parameters ($I = 3$) for
 606 the horizontal GNSS-A data, vertical GNSS-A data, and other data. The initial observational
 607 errors were given as follows:

$$\left(\sigma_{\text{GNSS}_{\text{hor}}}^{\text{ini}}, \sigma_{\text{GNSS}_{\text{ver}}}^{\text{ini}}, \sigma_{\text{OBP}_1}^{\text{ini}}, \sigma_{\text{OBP}_2}^{\text{ini}}, \sigma_{\text{GNSS-A}_{\text{hor}}}^{\text{ini}}, \sigma_{\text{GNSS-A}_{\text{ver}}}^{\text{ini}} \right) = \quad (30)$$

$$(2.5, 5, 10, 2.5, 20, 20) \text{ [cm]}.$$

608 The onshore GNSS data potentially had standard deviations of a few centimeter as the
 609 observational errors from the previous geodetic slip inversion studies [Inuma et al., 2012;
 610 Tomita et al., 2020]. The observational errors for OBP₁ [Maeda et al., 2011] and OBP₂ [Ito et al.,
 611 2011] were roughly given from measurement errors following Inuma et al. [2012]. We provided
 612 relatively small observational errors for the GNSS-A data compared with the instrumental
 613 measurement errors (from several tens of centimeters [Sato et al. 2011] to ~1 meter [Kido et al.,
 614 2011]). We then assigned the initial observational covariance matrices $\mathbf{E}_i^{\text{ini}} (i = 1, \dots, 3)$
 615 following Equation (30). Meanwhile, as for the ABIC-LSM, a diagonal observational covariance
 616 matrix was given based on the following relative observational errors:

$$\sigma_{\text{GNSS}_{\text{hor}}} : \sigma_{\text{GNSS}_{\text{ver}}} : \sigma_{\text{OBP}_1} : \sigma_{\text{OBP}_2} : \sigma_{\text{GNSS-A}_{\text{hor}}} : \sigma_{\text{GNSS-A}_{\text{ver}}} = 1 : 2 : 2 : 1 : 10 : 10. \quad (31)$$

617 Because the ABIC-LSM tends to generate larger misfits in the offshore area for the case of the
 618 2011 Tohoku-oki earthquake, we determined the relative observational errors by trial and error.

619 Figure 9 shows the estimated slip distributions and the estimation errors, and Figure 10
 620 shows percentile differences and histograms for the unknowns. Through the rj-MCMC method,
 621 the weighting parameters were determined as Figure 10c. Using the estimated weighting
 622 parameters (mean values of samples), the adjusted observational errors are obtained as follows:

$$\left(\sigma_{\text{GNSS}_{\text{hor}}}, \sigma_{\text{GNSS}_{\text{ver}}}, \sigma_{\text{OBP}_1}, \sigma_{\text{OBP}_2}, \sigma_{\text{GNSS-A}_{\text{hor}}}, \sigma_{\text{GNSS-A}_{\text{ver}}} \right) \quad (32)$$

$$= \left(10^{-\frac{\Lambda_1}{2}} \sigma_{\text{GNSS}_{\text{hor}}}^{\text{ini}}, 10^{-\frac{\Lambda_1}{2}} \sigma_{\text{GNSS}_{\text{ver}}}^{\text{ini}}, 10^{-\frac{\Lambda_1}{2}} \sigma_{\text{OBP}_1}^{\text{ini}}, 10^{-\frac{\Lambda_1}{2}} \sigma_{\text{OBP}_2}^{\text{ini}}, 10^{-\frac{\Lambda_2}{2}} \sigma_{\text{GNSS-A}_{\text{hor}}}^{\text{ini}}, 10^{-\frac{\Lambda_3}{2}} \sigma_{\text{GNSS-A}_{\text{ver}}}^{\text{ini}} \right)$$

$$= (2.47, 4.93, 9.86, 2.47, 177.32, 59.20) \text{ [cm]}.$$

623 The adjusted observational errors for the GNSS and OBP data did not significantly changed from
 624 the initial values, while those for the GNSS-A data indicated large uncertainties. Considering the
 625 instrumental measurement errors (from several tens of centimeters [Sato et al., 2011] to ~1 meter
 626 [Kido et al., 2011]) and the early postseismic displacements (especially affecting the horizontal
 627 components), the adjusted large observational errors for the GNSS-A data are reasonable.

628 Furthermore, histograms of the weighting parameters for the GNSS-A data show wide ranges
629 (Figure 10). This is because the total number of the GNSS-A data is small. Although previous
630 ABIC-LSM studies have often considered relative weights between different observational data
631 [e.g., Funning et al., 2014], the relative weights were finally fixed to certain values optimized by
632 the ABIC criterion. By contrast, the rj-MCMC method can obtain slip distributions considering
633 wide ranges of the weighting parameter through the MCMC sampling process.

634 Figure 9 shows that the slip distributions estimated by the rj-MCMC method were similar
635 to the slip distribution estimated by the ABIC-LSM, which show large coseismic slip over 20 m
636 at the up-dip portion of the plate interface in the off-Miyagi region (the central portion of the
637 fault zone, called as the main rupture area) and small coseismic slip less than 20 m at the down-
638 dip portion of the plate interface in the off-Fukushima region (the southern portion of the fault
639 zone, called as the sub-rupture area). These features are the same as previous studies [e.g., Yagi
640 & Fukahata, 2011; Iinuma et al., 2012; Ozawa et al., 2012; Yue & Lay, 2013].

641 Comparing the results of the ABIC-LSM and the rj-MCMC method, the rj-MCMC
642 method provided relatively large slip near the trench (Figure 9). This feature was the same as the
643 results of the synthetic tests (e.g., Figure 2). The estimation error maps (SD and NIQR) of the rj-
644 MCMC method demonstrate small errors just below the offshore observational sites and large
645 errors in the northern and southern portions of the main rupture area (especially, around 38.5°N
646 near the trench and around 37.5°N). These large estimation errors were caused by low spatial
647 resolution due to lack of offshore observational sites. We can find the low spatial resolution there
648 by checkerboard resolution tests (Figure 11a; Figure S11) and reconstruction ratio (Figure 11b).
649 In the checkerboard resolution tests, each slip patch has the slip amount of ~21.2 m, and size of
650 the slip patch is $\sim 80 \times 80 \text{ km}^2$. Moreover, Figure 10b and 10c demonstrate that large coseismic
651 slip with low probability was obtained in the areas with the large estimation errors as clearly seen
652 by difference between the 95th and 50th percentiles and by a histogram for the slip at sub-fault
653 C; i.e., the slip amount there was basically estimated to be zero, but it might be large in low
654 probability. Such high coseismic slip with low probability cannot be investigated by the
655 conventional ABIC-LSM because of its assumption that the estimation errors follow a Gaussian
656 distribution. Meanwhile, we can also find low spatial resolution in the sub-rupture area (Figure
657 11b). However, unlike the large estimation error areas around the main rupture area, quite large
658 coseismic slip did not be sampled (Figure 10b and Figure 10c for the sub-fault A). Thus, we

659 figured out that the sub-rupture did not reach high slip amount such as the main rupture, but
660 spatial extent of the sub-rupture might not be well constrained considering the low spatial
661 resolution.

662

663 **5 Summary**

664 In this study, we developed the trans-dimensional geodetic inversion approach using the
665 rj-MCMC method based on the Voronoi partition and assessed its performance by the five
666 synthetic tests and the application to the 2011 Tohoku-oki earthquake.

667 Throughout the synthetic tests and the application, the rj-MCMC method demonstrated
668 similar or superior performance compared with the conventional ABIC-LSM from the point of
669 view of reproducing fault slip distributions. Because of the absence of the smoothing constraints,
670 the rj-MCMC method can flexibly express fault slip distributions; both of the smooth and the
671 sharp fault slip distributions can be reproduced (e.g., synthetic tests 1 and 2), and the spatially
672 non-uniform degree of the fault slip smoothness can be expressed (e.g., site pattern 1 in synthetic
673 tests 1 and 4, showing the sharp down-dip limits of slip and the smooth up-dip slip limits of slip).
674 Especially in synthetic test 4, non-uniformness of the fault slip distributions reflected spatial
675 heterogeneity of the data sensitivity to fault slips depending on spatial coverage of observational
676 sites. Because geodetic observational data often have large variation of their spatial coverage as
677 shown in the application of the 2011 Tohoku earthquake, the rj-MCMC method is suitable to
678 handle such geodetic observational data for appropriately imaging a fault slip distribution following
679 the data sensitivity. Moreover, the rj-MCMC method can prevent the occurrence of the artificial
680 spotting slips that cannot be avoided by the conventional ABIC-LSM. This benefit is provided
681 due to sparsity of number of unknowns introduced by the Voronoi partition.

682 One of utilities of the MCMC sampling is in obtaining the estimation errors following a
683 non-Gaussian distribution. As shown in the synthetic tests and application (especially, synthetic
684 test 4 and application), we successfully obtained slip parameters following non-Gaussian
685 distributions, which cannot be expressed by the conventional ABIC-LSM. These non-Gaussian
686 estimation errors suggested further detailed information on fault slip behavior such as high
687 coseismic rupture or strong fault locking in regions with low spatial resolution, which are useful
688 for coupling risk assessment or evaluation of large co- and post-seismic fault slip events.

689 Meanwhile, we demonstrated utility of the percentile differences (e.g., Figures 3b, S4b, S5b and
690 10b) to roughly understand distributions of the estimation errors in map views.

691 For the conventional ABIC-LSM, the estimation error and spatial resolution are affected
692 by the prior information, such as the spatially uniform smoothing constraint; thus, they uniformly
693 vary depending on strength of the smoothing constraint. Although the *rj*-MCMC method also
694 have influence on the prior information, such as the Voronoi-partition assumption, we can easily
695 evaluate precision of the unknowns from standard deviation, NIQR, or PDF histograms of the
696 MCMC samples without such spatial uniform dependency. Meanwhile, it is difficult to assess
697 spatial resolution (i.e., sensitivity of the observational data to fault slips) from a series of the
698 samples obtained by performing the *rj*-MCMC method once. To assess this, it is effective to
699 conduct the checkerboard resolution tests (Sections 3.7 and 4). We also introduced an indicator
700 of the reconstruction ratio averaging various patterns of the checkerboard resolution tests and
701 demonstrated its usefulness in considering the spatial resolution.

702 Our results also showed utility of the weighting (hierarchical scaling) parameters
703 implemented in the MCMC sampling. As shown in synthetic test 3, the weighting parameters can
704 appropriately adjust the initial observational errors to the given observational errors. The
705 adjustment of the observational errors provided us reasonable fault slip distributions. Moreover,
706 as the weighing parameters were sampled through the MCMC procedure as well as the other
707 unknowns, we can obtain the estimated slip distributions considering the possible extents of the
708 weighting parameters as shown in the weighting parameter histograms (e.g., Figures 3c, S4c,
709 S5c, and 10c). This is one of advantage of the MCMC method compared with ABIC-LSMs that
710 can adjust relative weighting parameters but cannot consider their possible extents. Furthermore,
711 we can easily handling multiple weighting parameters. These flexibilities of the weighting
712 parameters are quite useful for modeling geodetic data that included various kinds of
713 measurements as shown in the application to the 2011 Tohoku earthquake.

714 As indicated above, the developed *rj*-MCMC method has various advantages compared
715 with the conventional ABIC-LSMs; therefore, we conclude that it is effective for inverting
716 geodetic observational data into fault slips. The *rj*-MCMC method can be widely used for
717 estimating coseismic slip distributions, postseismic slip distributions considering viscoelastic
718 Green's functions, coupling distributions, and it is useful to assess the detailed fault slip

719 behaviors even if the slip parameters follow non-Gaussian distributions and spatially non-
720 uniform roughness.

721

722 **Acknowledgments, Samples, and Data**

723 The plate models by Iwasaki et al. [2015] were constructed from topography and bathymetry
724 data by Geospatial Information Authority of Japan (250-m digital map), Japan Oceanographic
725 Data Center (500 m mesh bathymetry data, J-EGG500,
726 http://www.jodc.go.jp/jodcweb/JDOSS/infoJEGG_j.html), and Geographic Information Network
727 of Alaska, University of Alaska [Lindquist et al., 2004]. The figures were generated using
728 Generic Mapping Tools software [Wessel and Smith, 1998]. This research was supported by
729 Japan Society for the Promotion of Science (JSPS) KAKENHI (Grant Number: 20K14588).

730

731 **References**

- 732 Amey, R. M. J., Hooper, A., & Morishita, Y. (2019), Going to Any Lengths: Solving for Fault
733 Size and Fractal Slip for the 2016, Mw 6.2 Central Tottori Earthquake, Japan, Using a
734 Transdimensional Inversion Scheme. *Journal of Geophysical Research: Solid Earth*,
735 124(4), 4001–4016. [doi:10.1029/2018JB016434](https://doi.org/10.1029/2018JB016434)
- 736 Amey, R. M. J., Hooper, A., & Walters, R. J. (2018), A Bayesian Method for Incorporating Self-
737 Similarity Into Earthquake Slip Inversions. *Journal of Geophysical Research: Solid Earth*,
738 123(7), 6052–6071. [doi:10.1029/2017JB015316](https://doi.org/10.1029/2017JB015316)
- 739 Bayes, T (1763) An essay towards solving a problem in the doctrine of chances. *Philos Trans R*
740 *Soc Lond A*, 53:370–418
- 741 Bodin, T., & Sambridge, M. (2009), Seismic tomography with the reversible jump algorithm.
742 *Geophysical Journal International*, 178(3), 1411–1436. [doi:10.1111/j.1365-
743 246X.2009.04226.x](https://doi.org/10.1111/j.1365-246X.2009.04226.x)
- 744 Bodin, T., Sambridge, M., Gallagher, K., & Rawlinson, N. (2012), Transdimensional inversion
745 of receiver functions and surface wave dispersion. *Journal of Geophysical Research: Solid*
746 *Earth*, 117(B2). [doi:10.1029/2011JB008560](https://doi.org/10.1029/2011JB008560)

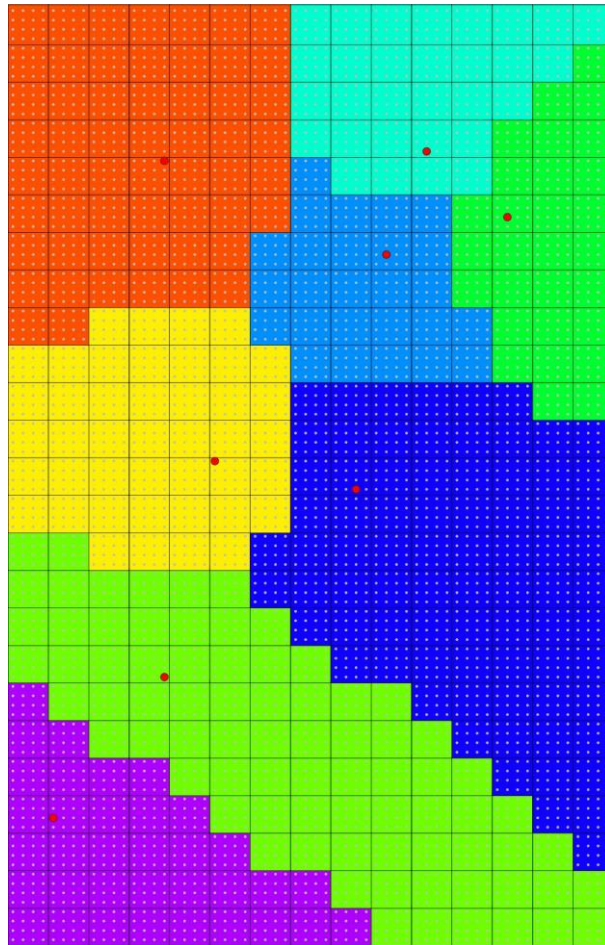
- 747 Brooks, S., Gelman, A., Jones, G., & Meng, X. L. (2011), Handbook of Markov chain Monte
748 Carlo. *Chapman & Hall/CRC*, New York.
- 749 Dettmer, J., Benavente, R., Cummins, P. R., & Sambridge, M. (2014), Trans-dimensional finite-
750 fault inversion. *Geophysical Journal International*, 199(2), 735–751.
751 [doi:10.1093/gji/ggu280](https://doi.org/10.1093/gji/ggu280)
- 752 Dettmer, J., Hawkins, R., Cummins, P. R., Hossen, J., Sambridge, M., Hino, R., & Inazu, D.
753 (2016), Tsunami source uncertainty estimation : The 2011 Japan tsunami. *Journal of*
754 *Geophysical Research: Solid Earth*, 121, 4483–4505. [doi: 10.1002/2015JB012764](https://doi.org/10.1002/2015JB012764).
- 755 Du, Y., Aydin, A., & Segall, P. (1992), Comparison of various inversion techniques as applied to
756 the determination of a geophysical deformation model for the 1983 Borah Peak earthquake.
757 *Bulletin of the Seismological Society of America*, 82(4), 1840–1866.
- 758 Evans, E. L., & Meade, B. J. (2012), Geodetic imaging of coseismic slip and postseismic
759 afterslip: Sparsity promoting methods applied to the great Tohoku earthquake. *Geophysical*
760 *Research Letters*, 39(11), 1–7. [doi:10.1029/2012GL051990](https://doi.org/10.1029/2012GL051990)
- 761 Fukuda, J., & Johnson, K. M. (2008), A fully Bayesian inversion for spatial distribution of fault
762 slip with objective smoothing. *Bulletin of the Seismological Society of America*, 98(3),
763 1128–1146. [doi:10.1785/0120070194](https://doi.org/10.1785/0120070194)
- 764 Funning, G. J., Fukahata, Y., Yagi, Y., & Parsons, B. (2014), A method for the joint inversion of
765 geodetic and seismic waveform data using ABIC : application to the 1997 Manyi, Tibet,
766 earthquake. *Geophysical Journal International*, 196, 1564–1579. [doi:10.1093/gji/ggt406](https://doi.org/10.1093/gji/ggt406)
- 767 Galetti, E., & Curtis, A. (2018), Transdimensional Electrical Resistivity Tomography. *Journal of*
768 *Geophysical Research: Solid Earth*, 123(8), 6347–6377. [doi:10.1029/2017JB015418](https://doi.org/10.1029/2017JB015418)
- 769 Green, P. J. (1995), Reversible jump Markov chain Monte Carlo computation and Bayesian
770 model determination. *Biometrika*, 82(4), 711–732. [doi:10.1093/biomet/82.4.711](https://doi.org/10.1093/biomet/82.4.711)
- 771 Hallo, M., & Gallovič, F. (2020), Bayesian Self-Adapting Fault Slip Inversion With Green's
772 Functions Uncertainty and Application on the 2016 Mw7.1 Kumamoto Earthquake.
773 *Journal of Geophysical Research: Solid Earth*, 125(3), e2019JB018703.
774 [doi:10.1029/2019JB018703](https://doi.org/10.1029/2019JB018703)
- 775 Hastings, W. K. (1970), Monte Carlo sampling methods using Markov chains and their
776 applications, *Biometrika*, 57, 97- 109, [doi:10.2307/2334940](https://doi.org/10.2307/2334940).

- 777 Hawkins, R., Bodin, T., Sambridge, M., Choblet, G., & Husson, L. (2019), Trans-Dimensional
778 Surface Reconstruction With Different Classes of Parameterization. *Geochemistry,*
779 *Geophysics, Geosystems*, 20(1), 505–529. doi:10.1029/2018GC008022
- 780 Hawkins, R., & Sambridge, M. (2015), Geophysical imaging using trans-dimensional trees.
781 *Geophysical Journal International*, 203, 972–1000. doi:10.1093/gji/ggv326
- 782 Herman, M. W., Furlong, K. P., & Govers, R. (2018), The Accumulation of Slip Deficit in
783 Subduction Zones in the Absence of Mechanical Coupling: Implications for the Behavior
784 of Megathrust Earthquakes. *Journal of Geophysical Research: Solid Earth*, 123(9), 8260–
785 8278. doi:10.1029/2018JB016336
- 786 Hori, M. (2001), Inverse analysis method using spectral decomposition of Green's function.
787 *Geophysical Journal International*, 147(1), 77–87. doi:10.1111/j.1365-246X.2001.00505.x
- 788 Iinuma, T., Hino, R., Kido, M., Inazu, D., Osada, Y., Ito, Y., Ohzono, M., Tsushima, H., Suzuki,
789 S., Fujimoto, H., & Miura, S. (2012), Coseismic slip distribution of the 2011 off the Pacific
790 Coast of Tohoku Earthquake (M9.0) refined by means of seafloor geodetic data. *Journal of*
791 *Geophysical Research: Solid Earth*, 117, B07409. doi:10.1029/2012JB009186
- 792 Ito, Y., Tsuji, T., Osada, Y., Kido, M., Inazu, D., Hayashi, Y., Tsushima, H., Hino, R., &
793 Fujimoto, H. (2011), Frontal wedge deformation near the source region of the 2011
794 Tohoku-Oki earthquake. *Geophysical Research Letters*, 38, L00G05.
795 doi:10.1029/2011GL048355
- 796 Iwasaki, T., Sato, H., Shinohara, M., Ishiyama, T. & Hashima, A. (2015), Fundamental structure
797 model of island arcs and subducted plates in and around Japan, *2015 Fall Meeting,*
798 *American Geophysical Union*, San Francisco, Dec. 14-18, T31B-2878.
- 799 Kido, M., Osada, Y., Fujimoto, H., Hino, R., & Ito, Y. (2011), Trench-normal variation in
800 observed seafloor displacements associated with the 2011 Tohoku-Oki earthquake.
801 *Geophysical Research Letters*, 38, L24303. doi:10.1029/2011GL050057
- 802 Kimura, H., Tadokoro, K., & Ito, T. (2019), Interplate Coupling Distribution Along the Nankai
803 Trough in Southwest Japan Estimated From the Block Motion Model Based on Onshore
804 GNSS and Seafloor GNSS/A Observations. *Journal of Geophysical Research: Solid Earth*,
805 124(6), 6140–6164. doi:10.1029/2018JB016159

- 806 Kubo, H., Asano, K., Iwata, T., & Aoi, S. (2016), Development of fully Bayesian multiple-time-
807 window source inversion. *Geophysical Journal International*, 204(3), 1601–1619.
808 [doi:10.1093/gji/ggv540](https://doi.org/10.1093/gji/ggv540)
- 809 Lindquist, K. G., K. Engle, D. Stahlke, and E. Price (2004), Global Topography and Bathymetry
810 Grid Improves Research Efforts, *Eos Trans. AGU*, 85(19), 186.
- 811 Lubis, A. M., Hashima, A., & Sato, T. (2013), Analysis of afterslip distribution following the
812 2007 September 12 southern Sumatra earthquake using poroelastic and viscoelastic media.
813 *Geophysical Journal International*, 192(1), 18–37. [doi:10.1093/gji/ggs020](https://doi.org/10.1093/gji/ggs020)
- 814 Maeda, T., Furumura, T., Sakai, S., & Shinohara, M. (2011), Significant tsunami observed at
815 ocean-bottom pressure gauges during the 2011 off the Pacific coast of Tohoku Earthquake.
816 *Earth, Planets and Space*, 63(7), 803–808. doi:10.5047/eps.2011.06.005
- 817 Metropolis, N., Rosenbluth, A. W., Rosenbluth, M. N., Teller, A. H., & Teller, E. (1953),
818 Equations of state calculations by fast computing machines, *Journal of Chemical Physics*,
819 21, 1087-1092.
- 820 Minson, S. E., Simons, M., & Beck, J. L. (2013), Bayesian inversion for finite fault earthquake
821 source models I—theory and algorithm. *Geophysical Journal International*, 194, 1701–
822 1726. doi:10.1093/gji/ggt180
- 823 Miyazaki, S., McGuire, J. J., & Segall, P. (2011), Seismic and aseismic fault slip before and
824 during the 2011 off the Pacific coast of Tohoku Earthquake. *Earth, Planets and Space*, 63,
825 637–642. doi:10.5047/eps.2011.07.001
- 826 Okada, Y. (1992), Internal deformation due to shear and tensile faults in a half-space, *Bulletin of*
827 *the Seismological Society of America*, 82, 1018–1040.
- 828 Ozawa, S., Nishimura, T., Munekane, H., Suito, H., Kobayashi, T., Tobita, M., & Imakiire, T.
829 (2012), Preceding, coseismic, and postseismic slips of the 2011 Tohoku earthquake, Japan.
830 *Journal of Geophysical Research: Solid Earth*, 117, B07404. doi: 10.1029/2011JB009120
- 831 Jin, H., Kato, T., & Hori, M. (2007), Estimation of slip distribution using an inverse method
832 based on spectral decomposition of Green's function utilizing Global Positioning System
833 (GPS) data. *Journal of Geophysical Research*, 112, B07414. [doi: 10.1029/2004JB003378](https://doi.org/10.1029/2004JB003378)
- 834 Sambridge, M. (2013), A Parallel Tempering algorithm for probabilistic sampling and
835 multimodal optimization. *Geophysical Journal International*, 196(1), 357–374.
836 doi:10.1093/gji/ggt342

- 837 Sambridge, M., Gallagher, K., Jackson, A., & Rickwood, P. (2006), Trans-dimensional inverse
838 problems, model comparison and the evidence. *Geophysical Journal International*, 167(2),
839 528–542. [doi:10.1111/j.1365-246X.2006.03155.x](https://doi.org/10.1111/j.1365-246X.2006.03155.x)
- 840 Sato, M., Fujita, M., Matsumoto, Y., Ishikawa, T., Saito, H., Mochizuki, M., & Asada, A.
841 (2013), Interplate coupling off northeastern Japan before the 2011 Tohoku-oki earthquake,
842 inferred from seafloor geodetic data. *Journal of Geophysical Research: Solid Earth*,
843 118(7), 3860–3869. [doi:10.1002/jgrb.50275](https://doi.org/10.1002/jgrb.50275)
- 844 Sato, M., Ishikawa, T., Ujihara, N., Yoshida, S., Fujita, M., Mochizuki, M., & Asada, A. (2011).
845 Displacement Above the Hypocenter of the 2011 Tohoku-Oki Earthquake. *Science*,
846 332(6036), 1395. [doi:10.1126/science.1207401](https://doi.org/10.1126/science.1207401)
- 847 Somogyvári, M., & Reich, S. (2019), Convergence Tests for Transdimensional Markov Chains
848 in Geoscience Imaging. *Mathematical Geosciences*. [doi:10.1007/s11004-019-09811-x](https://doi.org/10.1007/s11004-019-09811-x)
- 849 Tomita, F., Iinuma, T., Ohta, Y., Hino, R., Kido, M., & Uchida, N. (2020), Improvement on
850 spatial resolution of a coseismic slip distribution using postseismic geodetic data through a
851 viscoelastic inversion. *Earth, Planets and Space*, 72(1), 84. [doi:10.1186/s40623-020-](https://doi.org/10.1186/s40623-020-01207-0)
852 [01207-0](https://doi.org/10.1186/s40623-020-01207-0)
- 853 Tomita, F., Kido, M., Ohta, Y., Iinuma, T., & Hino, R. (2017), Along-trench variation in seafloor
854 displacements after the 2011 Tohoku earthquake. *Science Advances*, 3, e1700113.
855 [doi:10.1126/sciadv.1700113](https://doi.org/10.1126/sciadv.1700113)
- 856 Watanabe, S. ichi, Sato, M., Fujita, M., Ishikawa, T., Yokota, Y., Ujihara, N., & Asada, A.
857 (2014), Evidence of viscoelastic deformation following the 2011 Tohoku-Oki earthquake
858 revealed from seafloor geodetic observation. *Geophysical Research Letters*, 41, 5789–
859 5796. [doi:10.1002/2014GL061134](https://doi.org/10.1002/2014GL061134)
- 860 Wessel, P., & Smith, W. H. F. (1998), New, improved version of the Generic Mapping Tools
861 released. *Eos Trans AGU*, 79(47):579
- 862 Xu, X., Sandwell, D. T., & Bassett, D. (2018), A spectral expansion approach for geodetic slip
863 inversion: implications for the downdip rupture limits of oceanic and continental
864 megathrust earthquakes. *Geophysical Journal International*, 212(1), 400–411.
865 [doi:10.1093/gji/ggx408](https://doi.org/10.1093/gji/ggx408)

- 866 Yabuki, T., & Matsu'ura, M. (1992), Geodetic data inversion using a Bayesian information
867 criterion for spatial distribution of fault slip. *Geophysical Journal International*, 109(2),
868 363–375. [doi:10.1111/j.1365-246X.1992.tb00102.x](https://doi.org/10.1111/j.1365-246X.1992.tb00102.x)
- 869 Yagi, Y., & Fukahata, Y. (2011), Rupture process of the 2011 Tohoku-oki earthquake and
870 absolute elastic strain release. *Geophysical Research Letters*, 38(19), 1–5.
871 [doi:10.1029/2011GL048701](https://doi.org/10.1029/2011GL048701)
- 872 Yokota, Y., Ishikawa, T., & Watanabe, S. (2018), Seafloor crustal deformation data along the
873 subduction zones around Japan obtained by GNSS-A observations. *Scientific Data*, 5,
874 180182. [doi:10.1038/sdata.2018.182](https://doi.org/10.1038/sdata.2018.182)
- 875 Yokota, Y., Ishikawa, T., Watanabe, S., Tashiro, T., & Asada, A. (2016), Seafloor geodetic
876 constraints on interplate coupling of the Nankai Trough megathrust zone. *Nature*, 534,
877 374–377. [doi:10.1038/nature17632](https://doi.org/10.1038/nature17632)
- 878 Yoshioka, S., Matsuoka, Y., & Ide, S. (2015), Spatiotemporal slip distributions of three long-
879 term slow slip events beneath the Bungo Channel, southwest Japan, inferred from
880 inversion analyses of GPS data. *Geophysical Journal International*, 201(3), 1437–1455.
881 [doi:10.1093/gji/ggv022](https://doi.org/10.1093/gji/ggv022)
- 882 Yue, H., & Lay, T. (2013), Source Rupture Models for the Mw 9.0 2011 Tohoku Earthquake
883 from Joint Inversions of High-Rate Geodetic and Seismic Data. *Bulletin of the*
884 *Seismological Society of America*, 103(2), 1242–1255. [doi:10.1785/0120120119](https://doi.org/10.1785/0120120119)
- 885
- 886
- 887
- 888
- 889
- 890
- 891



892

893

894 **Figure 1.** Image of the Voronoi partition

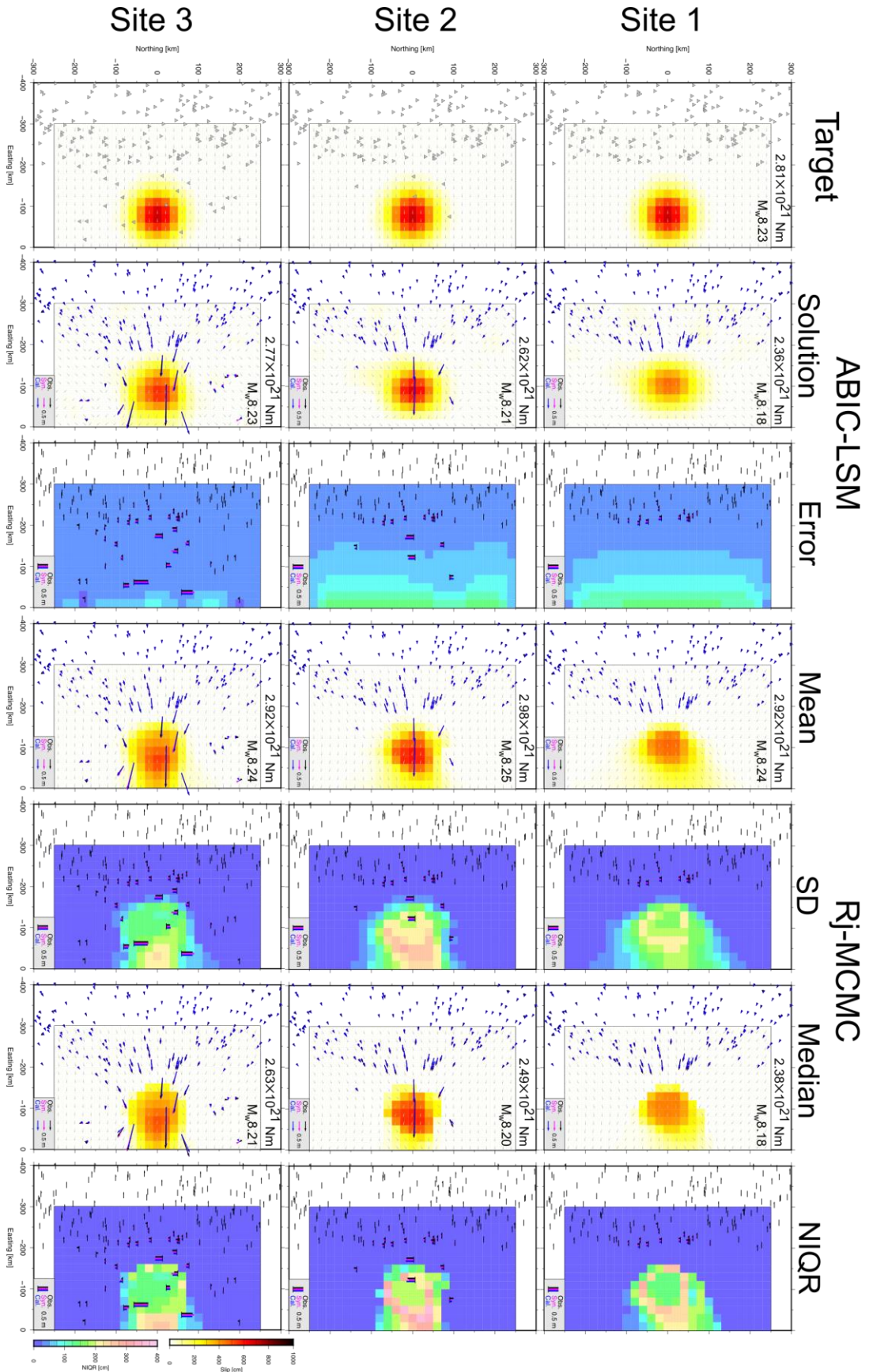
895 The whole rectangle represents a fault zone, and small squares represent sub-faults. Red

896 circles represent the Voronoi nuclei, and gray dots represent nucleus grid points (i.e., candidates

897 for the Voronoi nuclei). The colors of sub-faults indicate extents of the Voronoi cells classified

898 by the Voronoi nuclei.

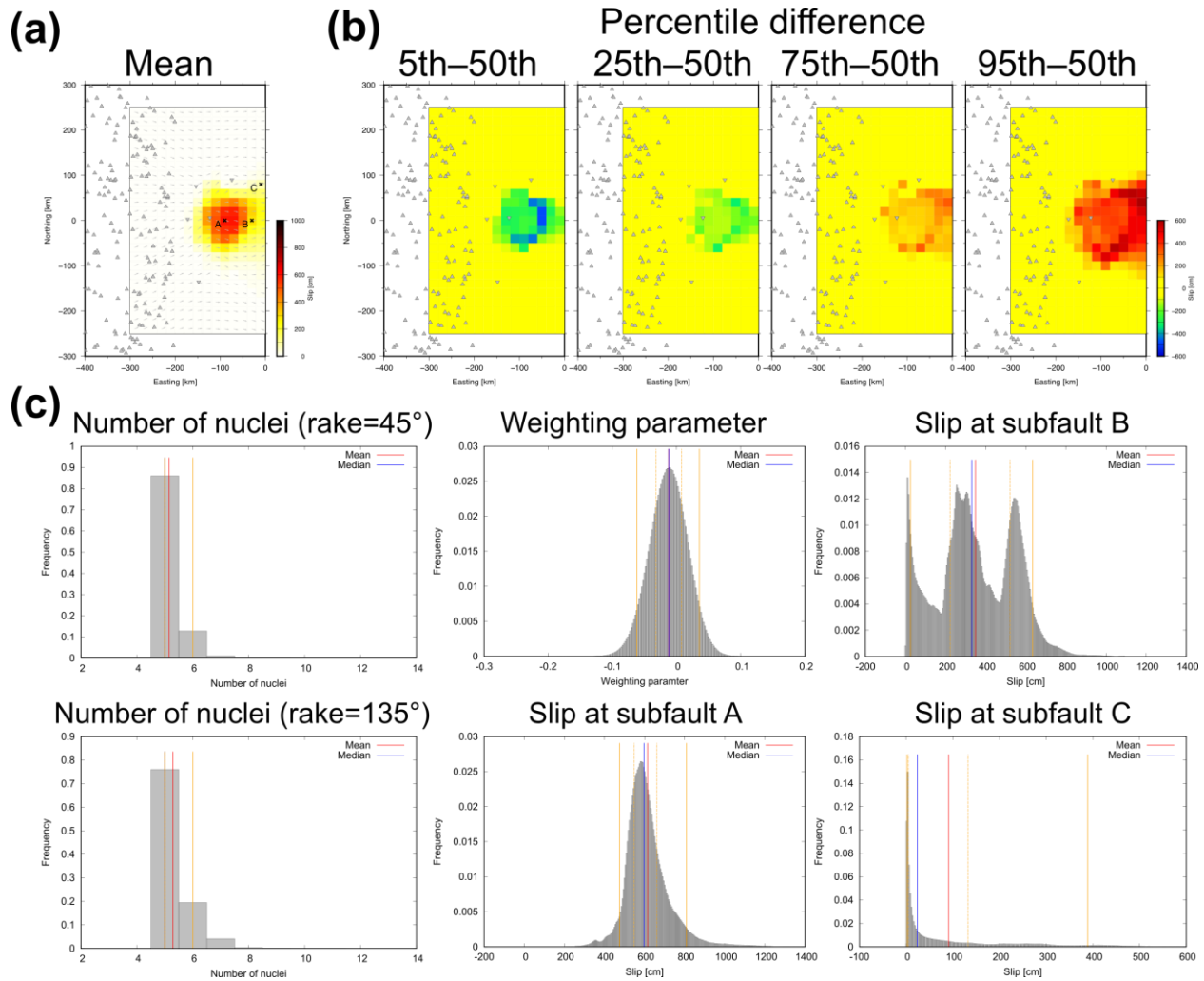
899



901
902
903
904
905
906
907
908
909
910
911
912
913
914
915
916
917

Figure 2. The estimated slip distributions and the estimation errors of synthetic test 1

The upper, middle, and lower panels show results of the synthetic test 1 assuming the site patterns 1, 2, and 3, respectively. Leftmost panels show the target slip distribution, and triangles and inverse triangles indicate synthetic onshore and offshore geodetic sites. The other panels show the estimated slip distributions and the estimation error distributions given by the ABIC-LSM and the rj-MCMC method (the mean and median models). Magenta, black, and blue vectors in the estimated slip distributions indicate the synthetic, and observed (synthetic displacements with observational noises), and calculated displacements in the horizontal components, respectively. The bars in the estimation error distribution indicate the displacements in the vertical component. Colors of the bars indicate the same meanings with the vectors.

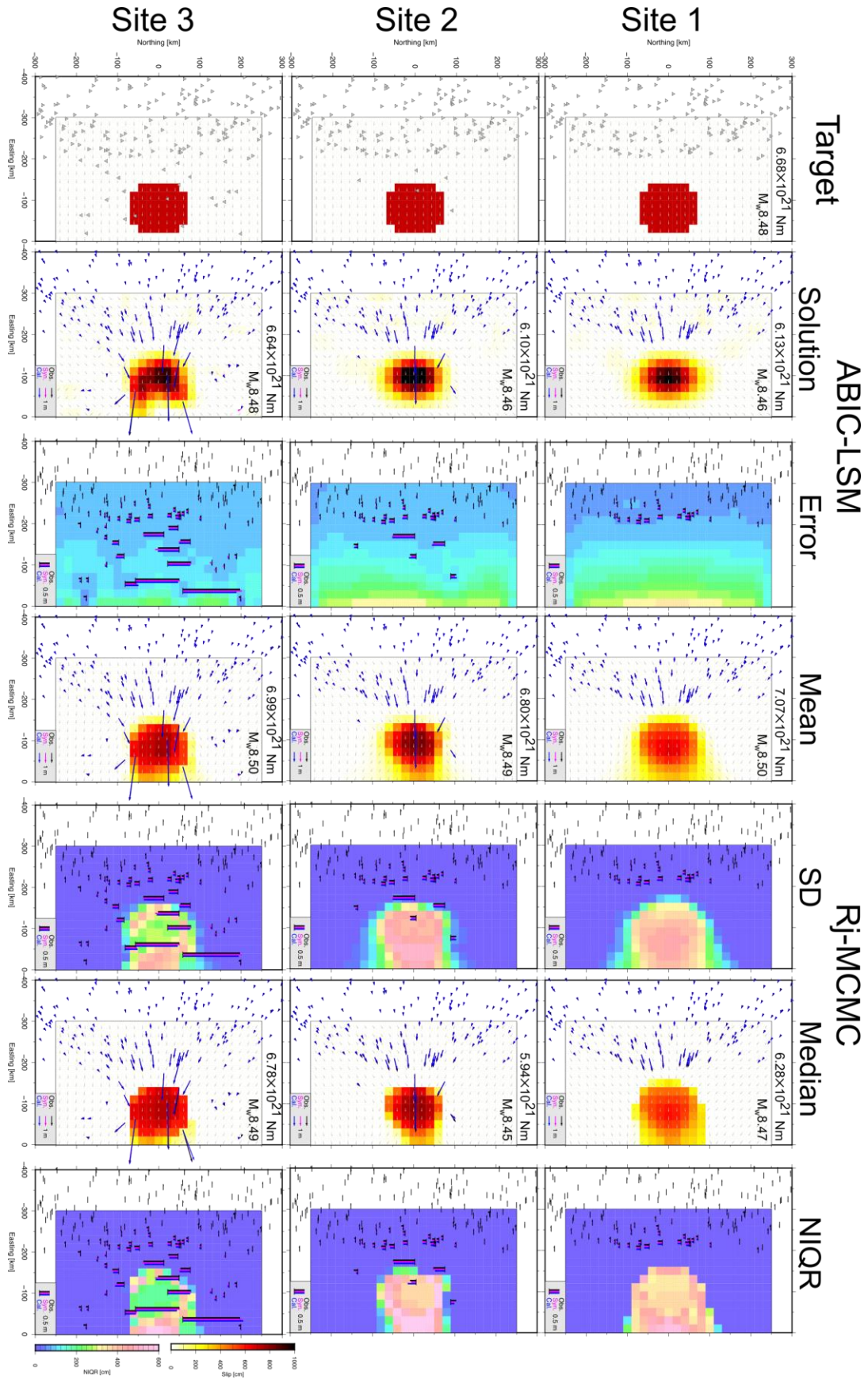


918

919

920 **Figure 3.** The percentile differences and the histograms for the synthetic test 1 assuming the site
 921 pattern 2

922 (a) The slip distribution estimated by the rj-MCMC method (the mean model) with the
 923 site distribution as shown in Figure 2. (b) The slip distributions for percentiles of 5th, 25th, 75th,
 924 and 95th subtracting 50th percentile (the median model). (c) The histograms for unknowns:
 925 number of the Voronoi nuclei for the fault slip component of rake=45°, that of rake=135°, the
 926 weighting parameter, and slips at sub-fault A, B, and C shown in (a). The vertical axis of each
 927 histogram indicate sample's frequency (i.e., number of the samples at certain range over total
 928 number of the samples). Red and blue vertical lines represent mean and median values,
 929 respectively. Solid orange vertical lines represent 5th and 95th percentile values, and dotted
 930 orange vertical lines represent 25th and 75th percentile values.



932

933 **Figure 4.** The estimated slip distributions and the estimation errors of synthetic test 2

934 The panels show results of the synthetic test 2 in the same manner as Figure 2.

935

936

937

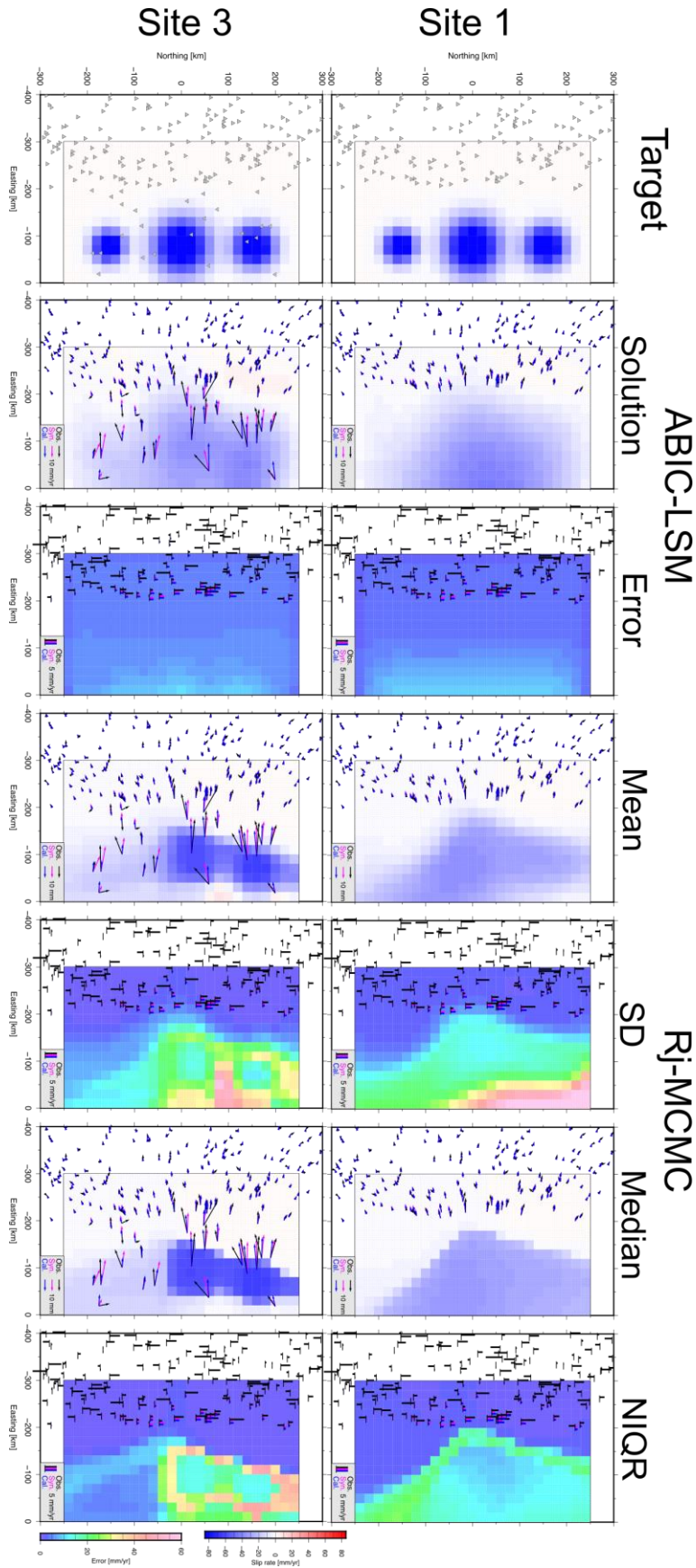
939

940 **Figure 5.** The estimated slip distributions and the estimation errors of synthetic test 3

941 The upper and lower panels show results of the synthetic test 3 assuming the smaller and
942 larger error cases, respectively. Leftmost panels show the target slip distribution, and triangles
943 and inverse triangles represent the same with Figure 2. The second and third columns show the
944 estimated slip distributions and the estimation error distributions given by the *rj*-MCMC method
945 with single weighting parameter, respectively. The fourth and fifth columns show the estimation
946 results given by the *rj*-MCMC method with dual weighting parameter. The vectors and bars are
947 written in the same manner as Figure 2.

948

949



951

952 **Figure 6.** The estimated slip distributions and the estimation errors of synthetic test 4

953 The upper and lower panels show results of the synthetic test 4 assuming the site patterns

954 1 and 3, respectively. The panels for each column show the results in the same manner as Figure

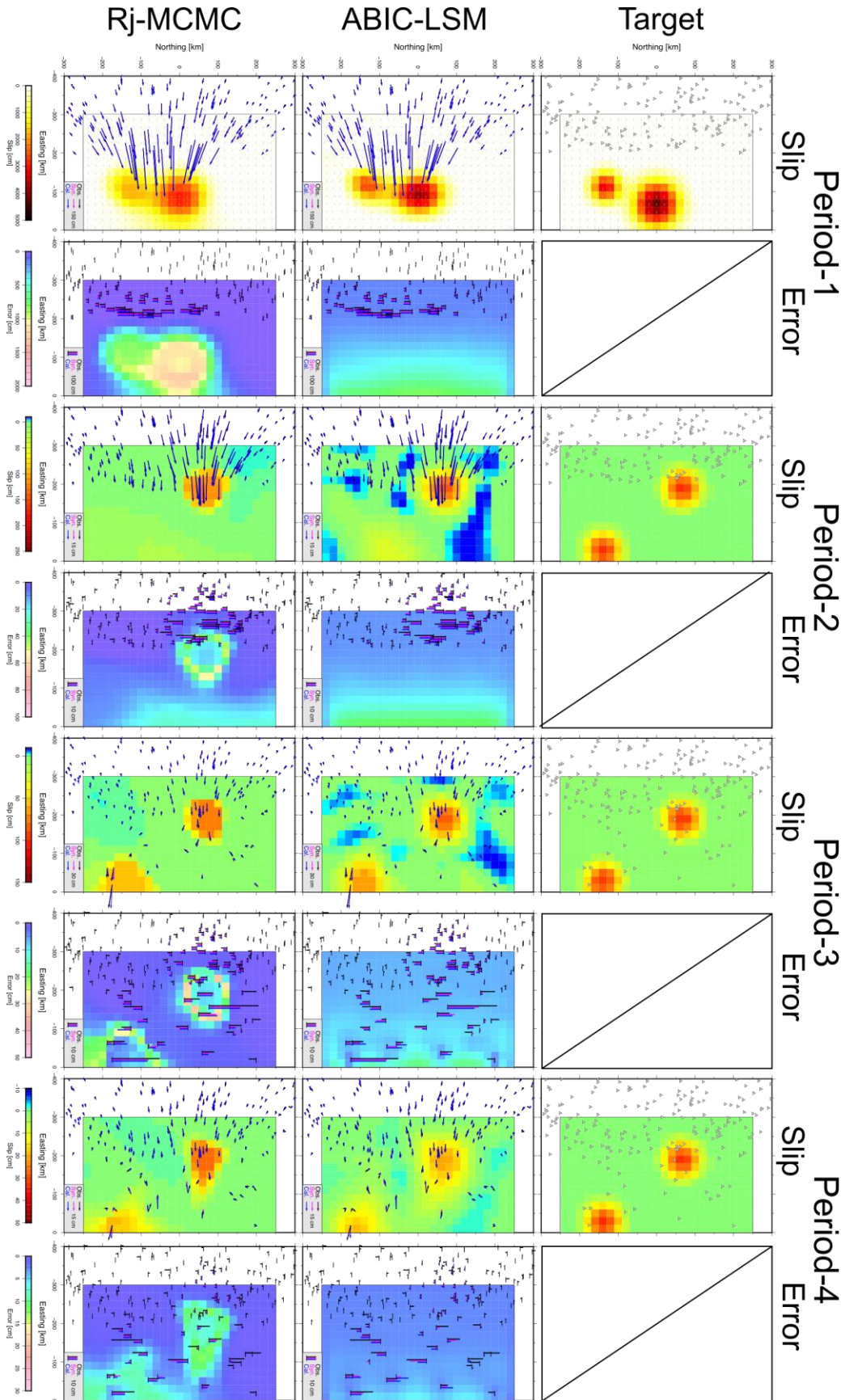
955 2.

956

957

958

959



961

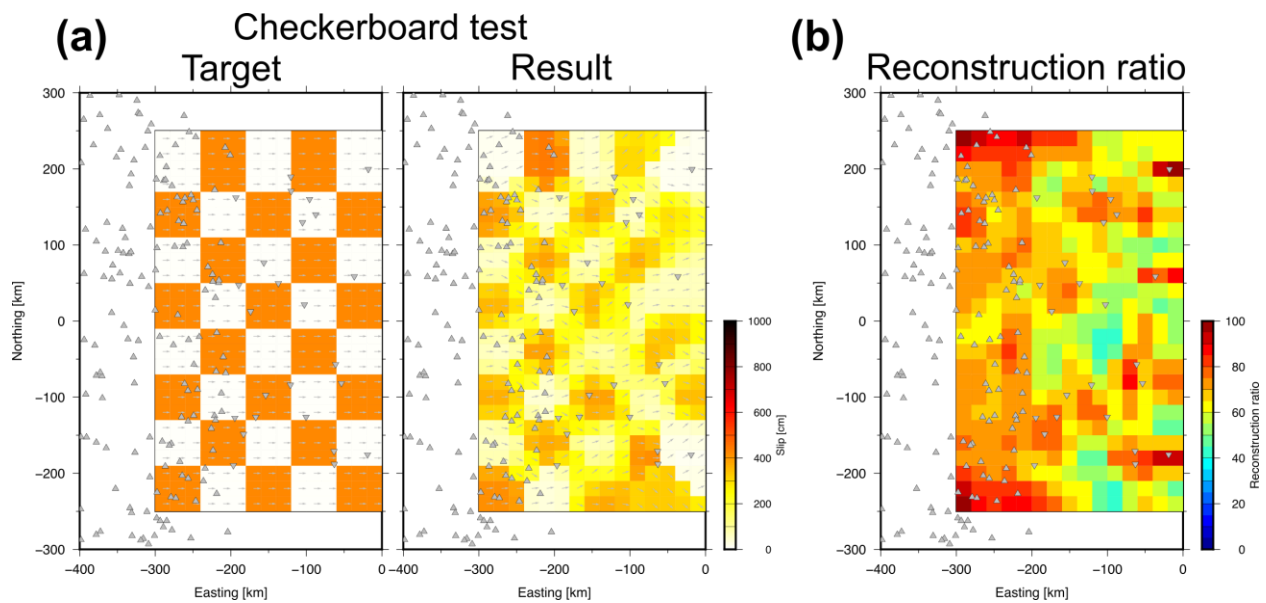
962 **Figure 7.** The estimated slip distributions and the estimation errors of synthetic test 5

963 The panels for each row show the target slip distributions and the estimation results for
 964 the periods 1–4. The upper panels show the target slip distributions. The middle and lower panels
 965 show results of the synthetic test 5 estimated by the ABIC-LSM and the rj-MCMC method,
 966 respectively. The vectors and bars are written in the same manner as Figure 2.

967

968

969



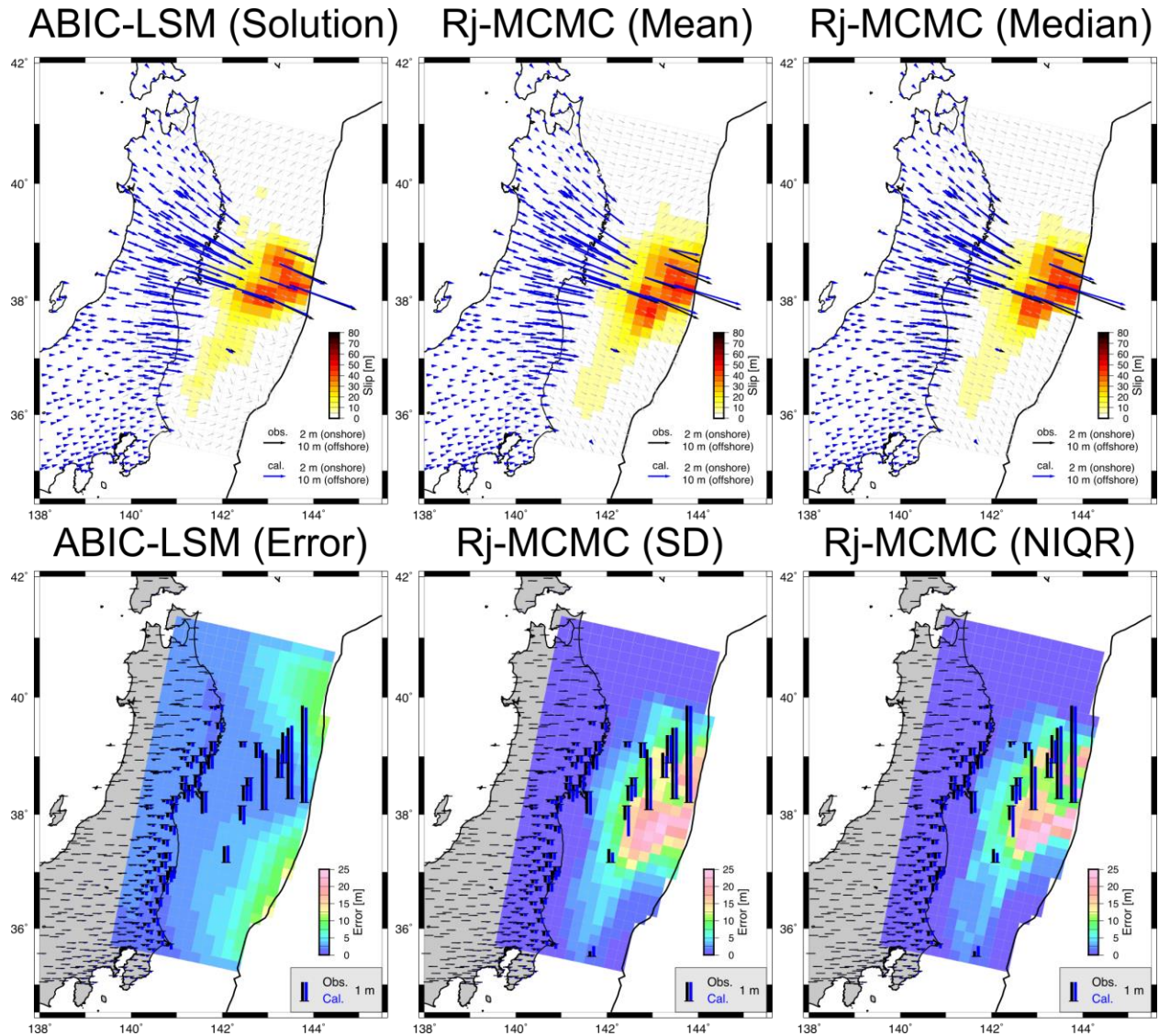
970

971 **Figure 8.** Example of the checkerboard resolution test and reconstruction ratio for the synthetic
 972 test 1

973 (a) The target and estimated slip distributions for one pattern of the checkerboard
 974 resolution tests. Triangles and inverse triangles represent the same with Figure 2. (b) Map of the
 975 reconstruction ratio averaging all patterns of the checkerboard resolution tests.

976

977



978

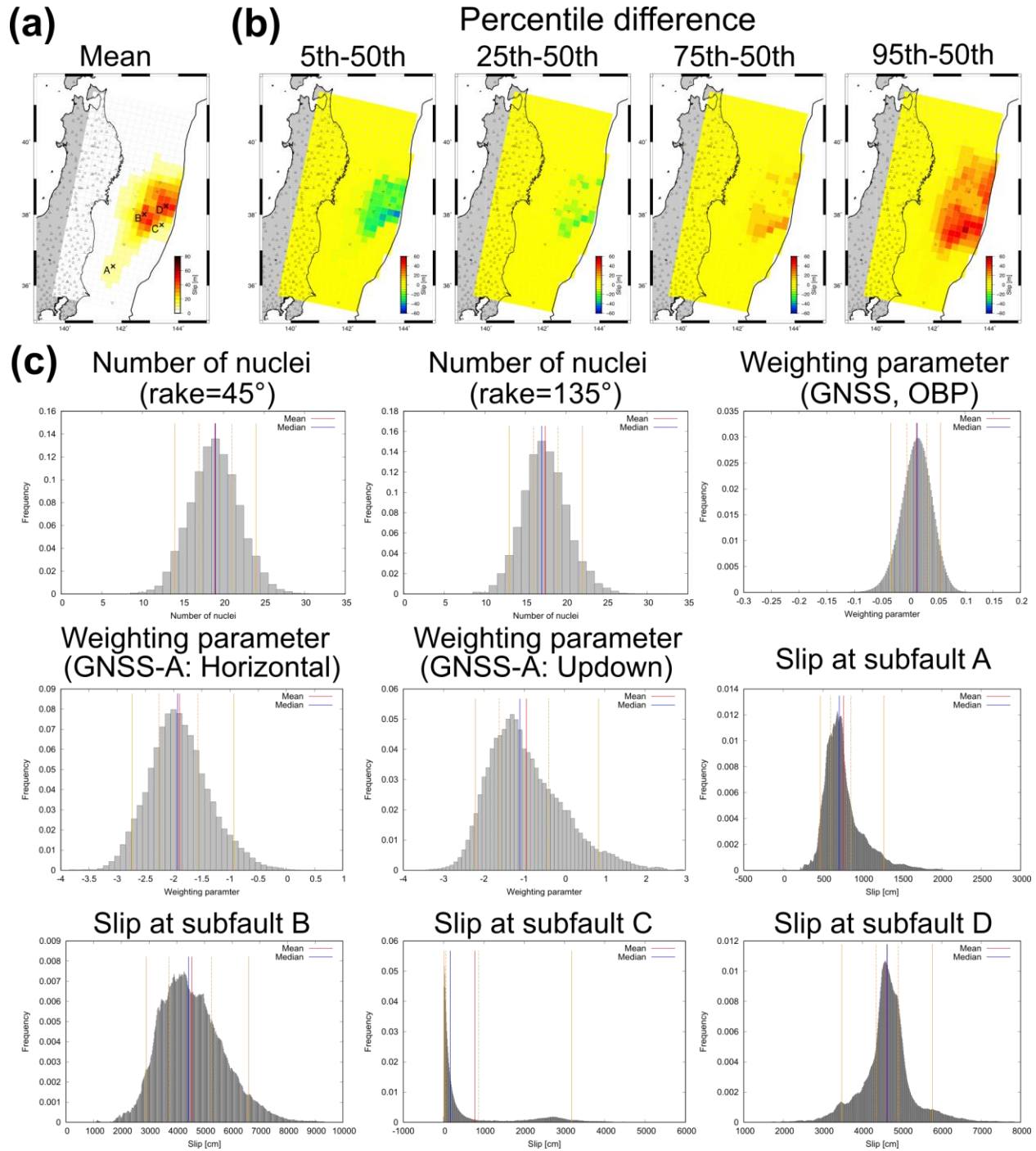
979

980 **Figure 9.** The estimated slip distributions and the estimation errors of the application

981 The upper and lower panels show the estimated slip distributions and the estimation error
 982 distributions of the 2011 Tohoku-oki earthquake, respectively. The first, second, and third rows
 983 show the results of the ABIC-LSM solution, the mean model of the rj-MCMC method, and the
 984 median model of the rj-MCMC method, respectively. The black and blue vectors represent the
 985 observed and calculated displacements in the horizontal components, respectively. The black and
 986 blue bars represent the observed and calculated displacements in the vertical component,
 987 respectively.

988

989



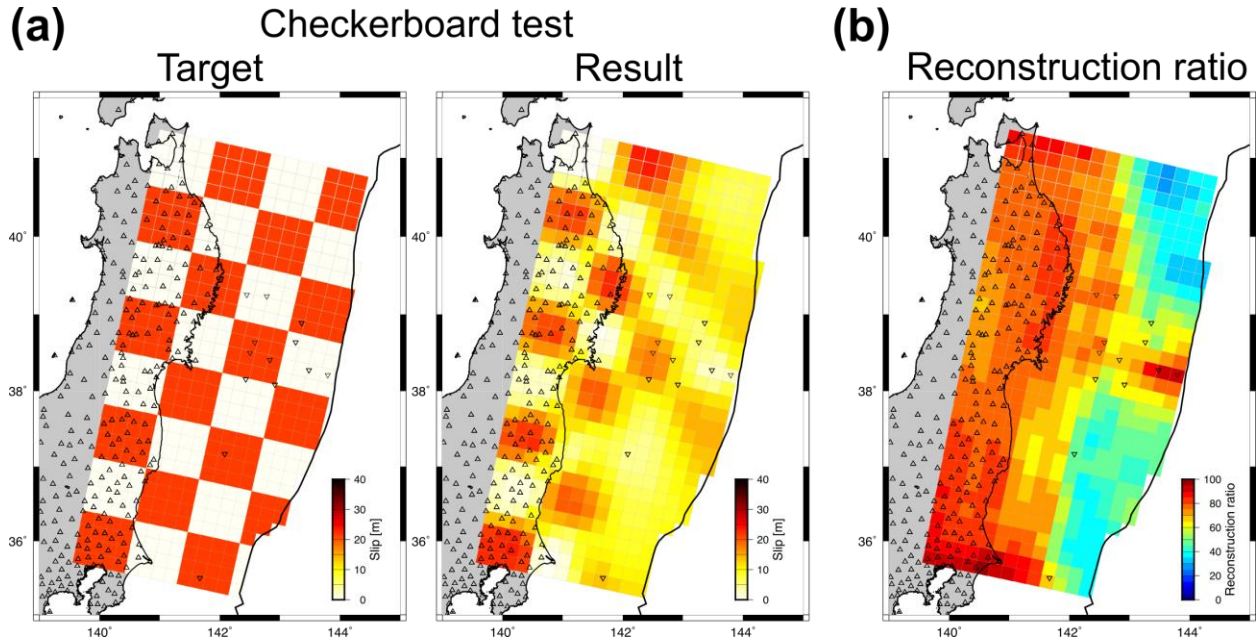
990

991

992 **Figure 10.** The percentile differences and the histograms for the application

993 (a) The slip distribution estimated by the rj-MCMC method (the mean model) with the
 994 site distribution as shown in Figure 9. (b) The panels show the percentile differences as the same
 995 manner with Figure 3. (c) The histograms for unknowns: number of the Voronoi nuclei for the

996 fault slip component of rake= 45° , that of rake= 135° , the weighting parameters, and slips at sub-
 997 fault A, B, C, and D shown in (a). The histograms are expressed in the same manner as Figure 3.



998

999

1000 **Figure 11.** Example of the checkerboard resolution test and reconstruction ratio for the 2011
 1001 Tohoku-oki earthquake

1002 (a) The target and estimated slip distributions for one pattern of the checkerboard
 1003 resolution tests. (b) Map of the reconstruction ratio averaging all patterns of the checkerboard
 1004 resolution tests.